
Wesleyan University

Exploring the Role of Environment in the Composition of ONC Proplyds

by

Jonas Powell
Class of 2019

A thesis submitted to the
faculty of Wesleyan University
in partial fulfillment of the requirements for the
Degree of Master of Arts

Middletown, Connecticut

April, 2018

*If people sat outside and looked at the stars each night,
I'll bet they'd live a lot differently.*

—CALVIN & HOBBES

Contents

1	Introduction	1
1.1	Submillimeter Observations	4
1.1.1	Interferometry	5
1.1.2	Continuum Emission	12
1.1.3	Line Emission	14
1.2	Disk & The Role of Environment	17
1.2.1	The Minimum Mass (Extra-)Solar Nebula	18
1.2.2	Low- and High-Mass Star Forming Regions	20
1.3	d253-1536: A Misaligned Binary System	24
1.3.1	Local Environment & Features	24
1.3.2	Previous Observations	26
1.4	Summary of Contents	29
2	Observations	30
3	Results	32
3.1	Cloud Contamination	32
3.2	Line Emission Statistics	34
4	Analysis	40
4.1	Gas Model	40
4.1.1	Establishing Physical Profiles	41
4.1.2	Generating a Model Image	44
4.2	Exploring Parameter Space	45
4.2.1	Grid Search	46

4.2.2	Markov Chain Monte Carlo	47
4.3	Fitting Procedure	50
4.3.1	$\text{HCO}^+(4-3)$ Fit	52
4.3.2	$\text{HCN}(4-3)$ Fit	53
4.3.3	$\text{CO}(3-2)$ Fit	54
4.4	Reflections on the Fits	55
5	Discussion	62
5.1	Physical Structure	62
5.1.1	Comparison to Binaries	68
5.2	Chemical Structures	73
5.3	Implications	78
6	Summary	82
Bibliography		84

Chapter 1

Introduction

Planetary systems, including our own Solar System, are born from circumstellar disks of gas and dust around young stars. Young ($\leq 10\text{Myr}$) circumstellar disks, known as protoplanetary disks, are easily distinguishable from their older siblings by their large abundance of gas, which typically outweighs the disk's dust by a factor of 100. However, as these disks age they are influenced by gravitational, chemical, radiative, and viscous forces, and their gas almost entirely dissipates as they become debris disks, much like our familiar Solar System's Kuiper Belt and asteroid belt. But while we can observe with relative ease the current state of our local planetary system and debris disks, understanding the process that brought us here is much more difficult. To do so, we must understand the nature of our own disk at its birth, and whether or not that process is a common one that we would expect to see replicated elsewhere. Unraveling this mystery requires that we turn to observations of other protoplanetary disks in order to develop a coherent narrative of disk evolution and, consequently, the conditions necessary for the formation of planetary systems like our own.

To understand the birth of our own protoplanetary disk, we must understand the birth of our Sun, as the two are intimately related. Stars form when a region of a molecular cloud develops a gravitational instability sufficient to lead to a runaway collapse (F. Shu, F. Adams 1987), helped along by macroscopic turbulence

in the cloud (McKee & Ostriker 2007). In this process, the cloud shrinks by a factor of around ten million on its way down to a star, analagous to shrinking a square the approximate size of Connecticut ($\sim 150 \times 150$ km) down to just 15mm on each side. Angular momentum, the product of a system's mass, velocity, and radial extent, must be conserved throughout this process, leading to a tremendous increase in the collapsing cloud's angular velocity. As the local material begins to self-gravitate, its center forms a dense core which will eventually become a young star¹.

However, if that angular momentum is conserved only through an increase in angular velocity, those velocities will become so large that the star itself will be unable to form, as centrifugal forces pulling outward will become more significant than the gravitation pulling the star in on itself. In order to prevent velocities from becoming this high, stellar jets and disks, made from the collapsing material, will develop to decentralize the system's mass and dissipate its angular momentum.

The resulting disks present flared radial structures, typically extending several hundred AU (Vicente & Alves 2005). Since these disks form directly out of the collapse process, they, like their stellar host and the original molecular cloud, are initially composed almost exclusively of molecular hydrogen (although their chemical evolution is significant and discussed more in §5). Temperatures in their outer regions ($r > 100$ au) are typically in the range of 10-100 K; gas masses are inferred to range from ones to tens of Jovian masses (Andrews & Williams 2005), although this value comes with significant uncertainty that is discussed in depth in §1.1.2 and §5. Masses for the disks in the present study are calculated in Chapter 3.

¹Binaries are also a common outcome in this process; according to Duchêne & Kraus (2013), approximately half of all stars are found with companions.

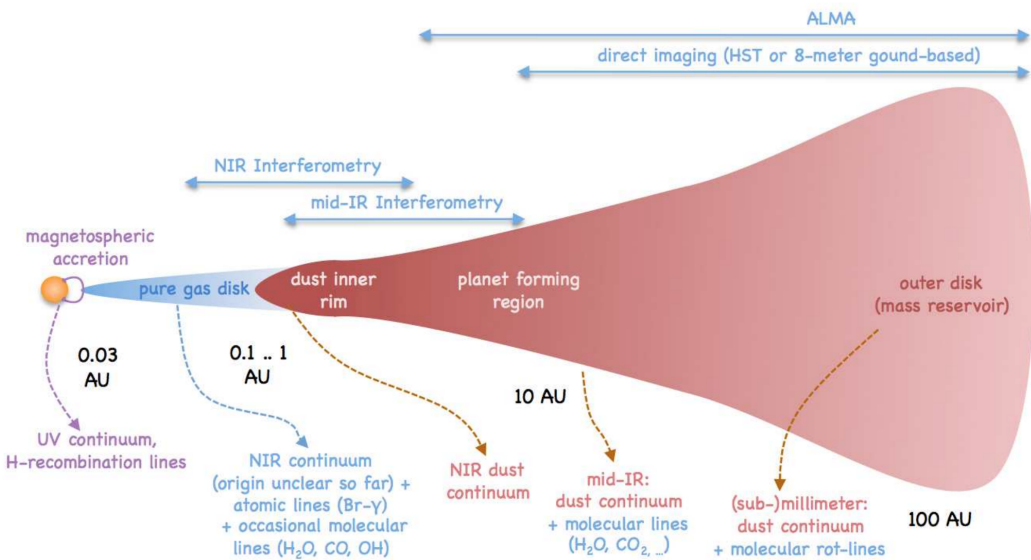


Figure 1.1: An edge-on slice of a protoplanetary disk is presented (Dullemond & Monnier 2010). As is visible in this graphic, significant radial segmentation of the disk exists, particularly between the inner gas disk and outer disk of gas, dust, and planetesimals. Also of note is the significant vertical flaring that occurs at large radii. The observations that this thesis are based on are sensitive primarily to the outer regions (tens to hundreds of au) of the disk.

By around 10-20 Myr, the primordial gas and dust in these disks becomes depleted through several processes, including accretion onto the host star, blowing out from radiation pressure, and becoming locked up in icy bodies, transitioning the disk from a protoplanetary disk to a debris disk. These debris disks are made up of what is thought to be second generation dust, created by the grinding down of boulders and planetesimals, since any primordial dust from the initial collapse should have been blown out by this time. The gas masses in debris disks tend to be orders of magnitude lower than in protoplanetary disks. For a more complete review of debris disks and their evolution, see Hughes et al. (2018).

1.1 Submillimeter Observations

Although protoplanetary disks' masses are dominated by gas, they still have sufficient dust to be optically thick in the optical. Consequently, mass measurements are not possible at optical wavelengths. However, since the optical depth of the dust at long (millimeter) wavelengths is low, and since the emission that we observe at these wavelengths is thermal rather than due to scattering (as it is in the optical), observations at millimeter wavelengths are preferred for measuring a disk's dust mass. In the radio, we may trace two types of emission:

- **CONTINUUM EMISSION:** Although the size distribution of grains in a dust disk is wide and heavily weighted towards smaller grains, larger, millimeter-sized grains are still present. These larger grains are far more efficient emitters in the radio, since the wavelength of a grain's peak thermal emission efficiency is approximately equal to its diameter. Thus, we may observe this continuum emission (so named thanks to the wide range of frequencies that it spans) from these millimeter-sized grains.

- LINE EMISSION: Because radial disk temperatures quickly fall below the temperatures required to cause photodissociation, molecules may live a stable existence in these disks. Conveniently, the rotational transitions of small molecules tend to emit at radio frequencies. Observations of the emission from these rotational transitions, known as line emission, can provide us with a wealth of important information, including kinematics, temperature information, disk chemistry and total disk mass.

Notably absent in both forms is emission from the central star. Since stars are hot, their emission peaks in the optical, and thus are extremely faint in the radio. Why, then, is the dust still bright relative to the star? While it's true that the flux *per area* of the dust is significantly smaller than of the star, the dust has a far greater surface area, allowing it to compensate and still be a bright emitter. Fig 1.2 (Hughes 2010) presents a spectral energy distribution, or SED, showing emission intensity as a function of wavelength from an imaginary disk system, demonstrating how small the star's flux density is at long wavelengths relative to the disk's contributions.

However, to understand these types of observation, one must first understand the nature of the telescope making the observations. What follows is a brief introduction to radio interferometry, followed by more complete explanations of continuum and line emission.

1.1.1 Interferometry

Interferometry is a clever way to make extremely high-resolution observations at long wavelengths without needing to use incredibly large collecting areas. Were one to naively attempt to create a “traditional” (single-aperture) telescope to

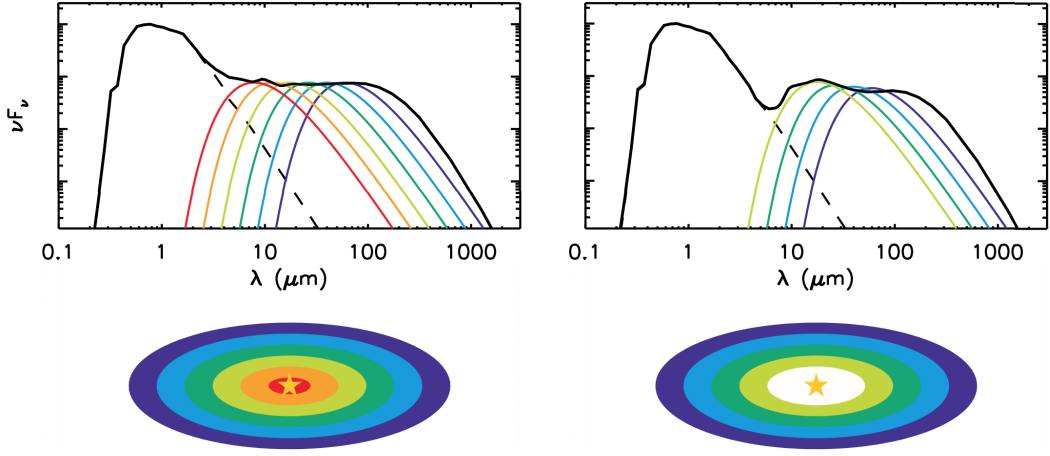


Figure 1.2: Two example SEDs, accompanied by cartoon models to illustrate the various contributions of different elements of a disk and their influences on the SED (Hughes 2010). The dashed line corresponds to emission from the stellar photosphere, while the colored lines are blackbody curves corresponding to emission from regions of the disk with different temperatures. Since radio observations take place at longer (hundreds to thousands of microns) wavelengths, one may easily see that the stellar contribution in that regime is minimal.

capture radio emission, they would quickly recall that, for a telescope with a single circular aperture of diameter D , maximum angular resolution is given by

$$\theta = 1.22 \frac{\lambda}{D}, \quad (1.1)$$

where θ is the angular resolution achieved, and λ is the wavelength of the emission being observed. Unfortunately for our naive telescope's angular resolution, light in the radio regime has wavelengths on the order of millimeters to centimeters, orders of magnitude longer than optical light, which is in the hundreds of nanometers. Consequently, to achieve a resolution comparable to that of an optical telescope, one would have to increase their aperture's diameter accordingly to match the increase in λ . Some have tried this approach: the Arecibo Observatory in Puerto Rico and the Five hundred meter Aperture Spherical Telescope in China (with

diameters of 300m and 500m, respectively) are two modern examples, but both still have resolutions ($\sim 25''$ for Arecibo and $\sim 15''$ for FAST, observing 3cm emission) that are too coarse to resolve the length-scales that we would like when observing disks (which are typically less than $10''$). Building and maintaining apertures this big is also a challenge, usually requiring mountains to be hollowed out, making this an unappealing solution unless their extremely large surface area (and the accompanying sensitivity) is absolutely necessary.

The alternative is to leverage the power of interferometry for a solution to the problem. In an interferometric system, one may construct an image using the interference patterns between light received by two or more separate apertures. In this case, the maximum angular resolution becomes inversely proportional to the maximum distance, or *baseline*, between any two apertures, which can be made almost arbitrarily large. Interferometry does come with tradeoffs, however, the most notable of which is in sensitivity, since sensitivity is proportional to collecting area and each dish in an interferometer is typically fairly small. Additionally, interferometers also have inherent spatial filtering, meaning that they are not sensitive to flux from sources covering large angular scales. This is because the largest angular scale of a flux source that a telescope is sensitive to is inversely proportional to its smallest baseline. Since the collecting area of a single-aperture telescope is a continuous surface, its smallest “baseline” is essentially infinitely small (making it sensitive to arbitrarily-large flux sources). For an interferometer, however, that smallest baseline is typically ones to tens of meters. Therefore, interferometers are intrinsically unable to capture flux from sources with angular scales larger than λ/D_{\min} .²

²This can actually be an advantage, however, as it offers the opportunity to choose the length-scale being observed, i.e. remove cloud contamination (large scale structure) from an image of a disk (a small structure).

Radio emission’s long wavelengths make it particularly well-suited to interferometry. While interferometry can be done at optical wavelengths with CCDs, it is far more difficult to execute, as light must be forced to physically interact before reaching the sensor via a complex and extremely precise optical system. At longer wavelengths, however, heterodyne receivers may be used, making the task of interfering the signals a digital process, rather than a physical one. A heterodyne receiver records both the amplitude (analogous to the intensity that a CCD measures) and the phase of the signal it receives. Because the receiver captures phase information as well as amplitude, the signals from two dishes may be digitally interfered after being received. Physical features must be calibrated out, including phase delay caused by differences in line-of-sight path length from the source between the receivers, atmospheric effects, and instrumental phase delays. The result, for a single baseline, is a complex voltage pattern describing the amplitude and phase of the interference pattern between the signal each dish received. We call this voltage pattern a *visibility*.

The complete output from an interferometer is a collection of these visibilities. Taken together, they approximate the Fourier transform of the sky image. We say that this output lives in the “visibility domain”, which itself is a Fourier transform of the image domain. A single visibility relates to the full set of visibilities analogously to the relationship between a pixel and an image.

While the image domain has spatial dimensions (i.e. the xy plane), the visibility domain instead uses the uv plane. The uv plane is a wavelength-scaled $x - y$ coordinate system parallel to the sky in the direction of the target source. Here “wavelength-scaled” can be taken to mean that $u = X/\lambda, v = Y/\lambda$, where λ is the wavelength of observation and X and Y are the lengths of the x and y (i.e. north/south, east/west) components of the projected baseline. Thus, each

baseline samples a specific spatial frequency, given by $\theta = 1/\sqrt{u^2 + v^2}$. An interferometer may thus be represented on the uv plane as a scatter of points, with each point corresponding to the wavelength-scaled, target-projected, component distance between two receivers. The ideal aperture would completely fill the uv plane, so that every spatial frequency was sampled. However, since the number of baselines we may access is very limited (approximately the square of the number of antennae in an array), this is clearly an impossibility for an interferometer.³

However, the fact that the *projected* baseline is really what determines visibility’s location in the uv plane, rather than the baseline’s “true”, un-projected length, allows us to cleverly gain far more points in the uv plane than one might immediately expect. Since the Earth rotates throughout the night, the projection of a given baseline relative to the target source will change throughout the night as well. Consequently, by making observations over the course of a day⁴, many more points in the uv plane may be sampled, yielding a better-filled plane. This process is known as “Earth rotation aperture synthesis.”

We now consider how one might recover an image from a set of observed visibilities. In general, moving between frequency space and distance space is given by a simple Fourier transform. When applying this translation to telescopes, we consider the shape of the image produced by observation of a single point source directly on axis with the aperture. For a conventional telescope with a circular aperture, coverage in the uv plane is in the shape of a filled circle of constant amplitude. Translation to the image domain, via a Fourier transform of that shape, results in the familiar 2-D Airy Disk, the characteristic point-

³Of course, a single-aperture telescope does not have this problem since its uv plane is one continuous collecting area and thus can be seen as having infinite baselines and complete uv coverage.

⁴Since the atmosphere is transparent in the radio, observations may be taken throughout both the day and night.

spread function (PSF) of a single aperture convolved with a point source. With an interferometer, this process would be equally straightforward if the uv plane were fully sampled, but because it is not, the resulting image is instead a Fourier transform of all the points in the uv plane sampled by the baselines, and can take on a very complex shape⁵. However, while this shape is complex, it is still - as is the case in the optical - just a convolution of the point source with some PSF, only in this case the PSF is more complicated than an Airy function. As we increase the number of uv points sampled, the resulting image will increasingly approximate a bumpy and/or elongated Airy disk. In radio astronomy, we call this PSF the “dirty beam”.

When observing a source, we would like to find the true sky brightness pattern (i.e. the sky image). As described above, the Fourier transform of a set of visibilities is a convolution of the dirty beam with the true sky brightness pattern. Therefore, we would like to remove the dirty beam’s contributions to the image. The process of removing the influence of the dirty beam, and the artifacts it can introduce, is called deconvolution. In practice, this deconvolution process takes the form of some iterative algorithm that selectively removes the effects of the dirty beam. The curious reader is referred to the CLEAN algorithm (Hogbom 1974), the first and most popular deconvolution algorithm (and the one used in this work), as well as the maximum-entropy method (Wernecke & D’Addario 1977; Skilling & Bryan 1984). It is worth noting at this point, however, that due to the non-unique result that the imaging process yields and since the CLEAN algorithm is a non-linear process that does not preserve noise properties, all of

⁵ Additionally, thanks to the incomplete sampling of the uv plane, an infinite number of images could all be consistent with some given finite set of visibilities, although many of them would not be physically possible. The one we choose to look at is determined by our deconvolution process, but is not actually the true image.

our analysis is performed directly on the visibilities themselves, rather than the image. This means that the specific parametrization of CLEAN or any other step in the imaging process does not need to be perfect, since it is purely diagnostic or expository.

In summary, interferometry works by recording amplitude and phase information about some emission with many radio antennae and digitally interfering each antenna's signal with the signal received by every other antenna. Each of the resulting interference patterns is called a visibility, and represents a point in *uv* space. Translation from the visibility domain to the image domain involves taking the Fourier transform of the visibilities and deconvolving the dirty beam's influence.

Currently, the world's most advanced interferometer, and the source of this thesis's data, is the Atacama Large Millimeter/Submillimeter Array (ALMA), shown in Fig 1.3a. Built in the high Chilean desert at around 5,000 meters (16,000 feet), the \$1.4-billion array first opened its eyes for scientific observation in mid-2011, with funding from a global partnership between the European Space Agency, the United States, Canada, Japan, Taiwan, and South Korea, in collaboration with the Republic of Chile. With its 66 total antennae (50 12-meter dishes and 16 7-meter dishes) and baselines extending out to 15 kilometers, it offers at least an order of magnitude increase in sensitivity and resolution over previous arrays that observe at similar frequencies, including the Submillimeter Array (8 6-meter dishes), NOEMA (10 15-meter dishes) and the CARMA (23 dishes of 3.5-meter, 6.1-meter, and 10.4-meter diameters).

The effects of this increase are impressive; gaps and rings in faraway disks can now be resolved in striking clarity (Fig. 1.3b), providing a treasure-trove of opportunity to hone our understanding of disk evolution and planetary-system

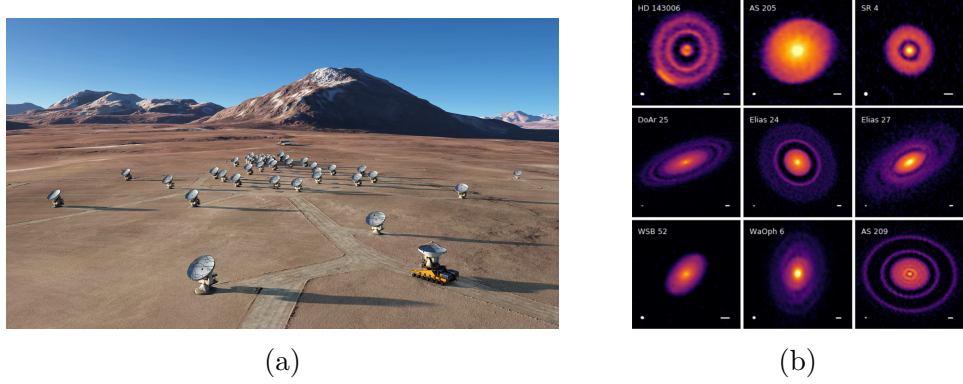


Figure 1.4: *Left:* A rendering of ALMA⁶ shows the interferometer’s antennae in the high desert, as well as a purpose-built truck moving one of the antennae (lower right). *Right:* A recent survey from ALMA by Andrews et al. (2018) reveals stunning detail in several protoplanetary disks.

formation. ALMA has also been a blessing to other subfields of astronomy as well, enabling high-resolution observations of everything from complex organic molecules in disks (Walsh et al. 2016; Podio et al. 2019) to gravitational lensing from dark matter halos (Herrera-Martín et al. 2019) to molecular tori around black holes (Combes et al. 2018). Additionally, as a component of the Event Horizon Telescope, ALMA played a key role in imaging a black hole’s event horizon for the first time (Collaboration 2019). These awe-inspiring projects are a small portion of ALMA’s contributions to the world of radio astronomy, and more are being made with each passing day.

With an improved understanding of the mechanics of radio interferometry, we may now revisit continuum and line emission.

1.1.2 Continuum Emission

Continuum emission observations integrate flux from a wide band of frequencies, just as our eyes do in the optical. They are appealing for their simplicity and because, by integrating a wide band, they are sensitive to faint objects.

When observing protoplanetary disks, an understanding of planet formation is often a guiding motivation. One parameter that is critical to the planet-forming process is total disk mass. We know that, to first order, when a disk is optically thin, its total mass, M_{disk} , is linearly proportional to its flux density, F_ν (Hildebrand 1983), which is found from an observation of continuum emission. This relationship is given by

$$M_{\text{dust}} = \frac{F_\nu d^2}{\kappa_\nu B_\nu(T_c)}, \quad (1.2)$$

where d is the source's distance, κ_ν is an assumed dust opacity, and $B_\nu(T_c)$ is the Planck function at a given characteristic temperature, T_c . The values of T_c and κ_ν can be inferred without much difficulty by fitting the disk's SED using a simple model. This function is, of course, rather approximate; it assumes a single temperature and single dust opacity (a function of composition and grain size distributions) throughout the disk. The assumption of optically thin emission means that calculations made will inherently be lower limits, since any substantial optical depth will block emission from inner regions of the disk. Furthermore, even in the case of optically thin emission, significant mass may be locked up in bodies that are invisible to our observations.

Traditionally, studies have used observed continuum fluxes to estimate dust mass and then inferred a total gas mass by assuming a 100:1 gas/dust ratio, based on the ratio observed in warm ISM clouds. However, it has been shown (e.g Miotello et al. 2016; Miotello 2017) that this value is highly variable, often falling closer to 10. Additionally, Liu et al. (2018) found that a ratio of 100 provoked instability (as measured by the Toomre criterion) in their smoothed-particle hy-

drodynamic simulation of the MWC 480 disk; instead, they found that values of 6-12 yielded their best results. The evidence for this variability is discussed in more depth in §5, but in short, the use of this ratio introduces a significant source of uncertainty, possibly of up to two orders of magnitude, into existing calculations of gas mass in protoplanetary disks based that are based on continuum emission.

1.1.3 Line Emission

As molecules collide with one another or absorb light, they gain energy, entering higher rotational energy states. However, they soon de-excite from the higher state, with a probability given by their specific Einstein coefficient. This de-excitation process - stepping down from one rotational energy state to the one below - causes the emission of light. Every transition in every molecule emits at its own specific frequency, or rest frequency, making that transition identifiable to observers. We may observe a specific rotational transition from a single type of molecule by tuning our receiver to be sensitive to a very narrow window of frequencies immediately around the rest frequency of the transition of interest. This is known as a spectral window. The narrow range of frequencies at which a given molecular transition emits makes ALMA’s large sensitivity particularly crucial for observations of molecular lines at high spectral resolution or in rare species.

One immediate feature that line emission gives us access to is velocity information: since all emission should have a single frequency (the transition’s rest frequency), we immediately know that any variation from that central frequency is a result of Doppler shifting caused by line-of-sight velocity⁷. This allows us to make a “moment-one” map of emission, which shows the intensity-weighted

⁷Technically, the uncertainty principle tells us that a line will have some “natural” width, but this width is small compared to the Doppler width.

velocity structure of the disks (Fig 1.5).

Observations of line emission also give us information about both the temperature and density structures of the disk. However, in the case of optically thin emission, the two are degenerate, since an increase in either one will increase emission intensity. In this case, we may combine observations of multiple species to model the temperature structure of a disk. In the case of an optically thick line, however, the temperature and density are no longer degenerate, since all emission originates from the $\tau = 1$ surface, which removes density from the equation and gives us a value for the temperature at that point in the disk's vertical structure. This is valuable since the disk's vertical temperature profile varies significantly, with the surface notably warmer than the midplane.

Besides offering information about radial density and temperature profiles, line emission also provides another way of finding total disk mass. Like the initial cloud that the star and disk formed from, the vast majority of the disk's mass comes in its gas, and like that initial cloud, the vast majority of that gas is molecular hydrogen, or H_2 . However, since H_2 is a symmetric molecule and thus has no permanent dipole moment, it has no rotational transitions and does not emit in the radio, making it invisible to our instruments. As a consequence, we must instead observe emission from other molecules, make assumptions about those molecules' abundances relative to H_2 , and extrapolate the total disk mass.

To do so, one generally begins with CO, second most abundant molecule behind H_2 . Thanks to its abundance, as well as its relatively low excitation temperature, CO provides robust, bright emission. Drawing on measurements of CO/ H_2 ratios in warm dense cloud (?Fogel et al. 2011), we use a ratio of 1:10000, or 10^{-4} , to represent CO's relative abundance in protoplanetary disks, while for other, more complex molecules, relative abundances are generally drawn from the interstellar-

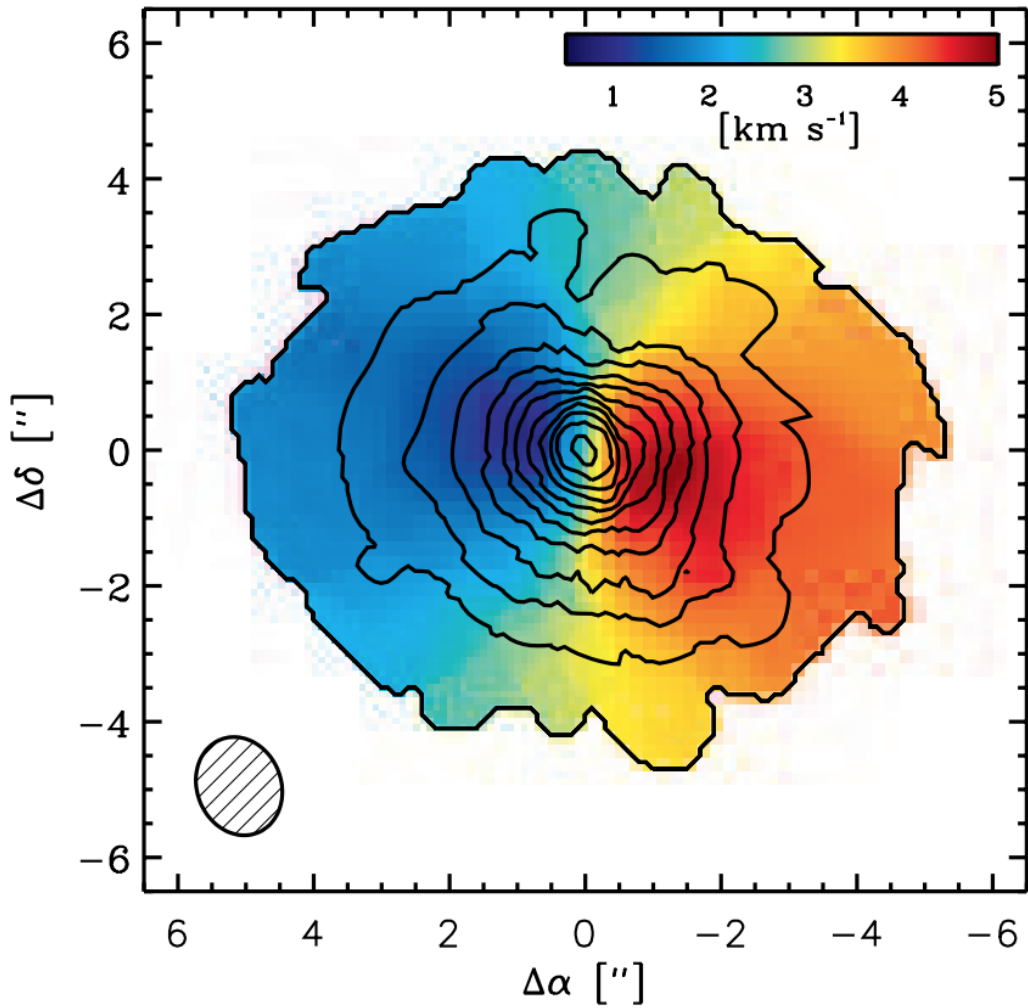


Figure 1.5: An example of a moment-one map of a protoplanetary disk, drawn from Rosenfeld et al. (2012). Colors correspond to intensity-weighted velocity; in other words, how quickly material is moving relative to the observer. One may consider this analogously to a spinning Frisbee, approaching the reader edge-on, where one half of the disk is spinning outwards (away from us) as the other side approaches. From this image, we immediately gain several pieces of information: for example, in this case, the disk as a whole is receding from view (since the velocity’s “zero point”, in yellow/green, is moving at 3 km/s), and that the disk’s eastern half is spinning away from us, while the western half comes towards us. This gives us a basic understanding of the disk’s kinematics.

medium literature and chemical modeling.

However, this CO/H₂ ratio of 10⁻⁴, which is frequently used to calculate total disk gas masses, comes with significant uncertainty. Using a gas-grain chemical model, Reboussin et al. (2015) showed, through an analysis of CO isotopologues, that at low temperatures (below 30-35K), CO is converted to less volatile molecules (typically s-CO₂ or s-CH₄). This means that below these temperatures, relative CO abundance quickly falls about two orders of magnitude below the literature value of 10⁻⁴. Schwarz et al. (2016) followed this modeling with high spectrospatial resolution ALMA observations of four CO isotopologues in the nearby protoplanetary disk TW Hya, and found a ratio of CO/H₂ = 10⁻⁶. Additionally, Yu et al. (2017) notes that CO depletion in the outer disk and optically thick emission from the inner disk has led observers (e.g. Ansdell et al. 2017, who found surprisingly low disk masses in their survey of ONC proplyds) to underestimate disk mass by more than an order of magnitude if they assume CO/H₂ = 10⁻⁴ and optically thin emission. They and Cleeves et al. (2015) also note that CO abundances change on short (~ 1 Myr) timescales, resulting in a degeneracy between disk age and mass. Ultimately, CO's tight dependence on disk temperature and its evolutionary trends with age increase the need for a well modeled temperature profiles to inform the selection of an appropriate molecular abundance of CO.

1.2 Disks & The Role of Environment

There is significant evidence that most stars in our galaxy (Lada & Lada 2003; Mann et al. 2015), including our own Sun (Gaidos et al. 2009; Tachibana et al. 2006), formed in high-mass star forming regions (SFRs). Therefore, understand-

ing our own creation story necessitates the understanding of protoplanetary disk evolution in these SFRs, and the role that environment plays in that process. However, until ALMA came online in 2012, line-emission studies of disks in these high-mass SFRs were not feasible, due to the need for increased sensitivity and resolution in the observations.

Now that this telescope is available, high-mass SFRs are open for observation. We may use this opportunity to try to better understand the role that environment plays in the development and evolution of protoplanetary disks, comparing them to the well-studied disk population in low-mass SFRs (Andrews & Williams 2005; Mann et al. 2015, e.g.) and the one well-characterized disk in a high-mass SFR (Factor et al. 2017), and evaluate how that environment may affect planet-formation potential.

1.2.1 The Minimum Mass (Extra-)Solar Nebula

The minimum-mass solar nebula (MMSN) is a conceptual aid used to inform astronomers about the distribution of material required to form a planetary system (Weidenschilling 1977). The MMSN is the radial density profile that our own Solar System would present if the mass of each planet were, rather than being bound up in spheres, instead ground up and spread across the ring bound by the orbits of their inferior and superior neighbors. Gas is then added to the ring until its gas:dust ratio reaches the canonical ISM value of 100:1 (meaning that gas giants like Jupiter would have very little gas mass added, while terrestrial planets like Earth would have their masses significantly increased). The resulting mass profile represents the minimum surface density required to form our own protoplanetary disk and thus a way to inform our comparisons of other disks to

our own. When this surface density profile is integrated into a single mass, it gives $M_{\text{MMSN}} = 0.01M_{\odot}$.

It is, of course, an extremely approximate characterization. One significant assumption it makes is that our planets formed in their current positions. This is a statement that we know both to be false (Tsiganis et al. 2005; Walsh et al. 2011) and consequential, since planetary migration can cause disks to lose mass by pushing competing planetesimals either out of orbit or into inner regions of the disk where they may be more susceptible to accreting onto the host star. Another assumption being made is that the chemistry is radially and temporally constant, which is also known to not be the case (van Dishoeck & Blake 1998).

The MMSN model was generalized to be tolerant to a wider diversity of planetary systems by Kuchner (2004) as the minimum-mass extrasolar nebula (MMEN), using 26 Doppler-detected planets in multi-planet systems to construct a disk analogous to that of the MMSN. Chiang & Laughlin (2013) developed a similar model, this time drawing on Kepler and HARPS planets ($n \approx 10^5$) to explain the existence of close-in ($P < 100$ days) super Earths, which make up approximately half of the planets observed in those catalogues. Both models assume that planets formed at or near their current positions. However, Raymond & Cossou (2014) showed, using 191 multi-planet systems primarily drawn from the Kepler catalogue, that the resulting range of surface density profiles was broad, and thus that using a single, “universal” profile to locate disks with planet-forming potential - as the MMSN/MMEN purports to offer - was not plausible. They note that this broad spread likely reflected the necessity for consideration of planet migration, particularly amongst gas giants.

Still, while the MMSN clearly makes significant assumptions that lead to inconsistencies, it is nonetheless used as an approximate barometer for planet-forming

potential.

1.2.2 Low- and High-Mass Star Forming Regions

Thanks to limitations in sensitivity and resolution, most submillimeter surveys in the pre-ALMA epoch focused on young disks in the nearby low-mass SFRs of Taurus-Auriga and ρ Ophiuchus. Dust-emission studies of disks in these regions by Andrews & Williams (2005, 2007) have yielded a wide range of disk masses, with a median of $0.005 M_{\odot}$ and a significant fraction with mass greater than the MMSN. This large fraction of disks with planet-forming potential is consistent with what we would expect based on the enormous number of exoplanets (as of this writing, the NASA Exoplanet Archive⁸ lists 3946 confirmed planets) that have been discovered in the last two decades.

Of course, studying only nearby disks paints an incomplete picture of the population and its evolutionary trends; for one, most stars form in high-mass SFRs (Lada & Lada 2003; Mann et al. 2015), and low-mass SFRs are qualitatively different than their high-mass siblings. High-mass SFRs are massive, dense clusters with large abundances of high-mass O and B stars. Protoplanetary disks in these regions experience accelerated mass loss, thanks to the powerful ionizing radiation from the high-mass stars (Anderson et al. 2013; Kalyaan et al. 2015; Xiao & Chang 2018). This mass loss is likely a problem for planet formation (Johnstone et al. 1998; Ovelar et al. 2012) and negatively affects potential habitability (Kruijssen & Longmore 2019), but its effects are not yet well understood. It is because of these factors that we would like to study disks in high-mass SFRs.

The nearest high-mass SFR to us is the Orion Nebula Cluster (ONC), 389 pc away (Gaia Collaboration et al. 2018). The Hubble Space Telescope was the first

⁸<https://exoplanetarchive.ipac.caltech.edu/index.html>

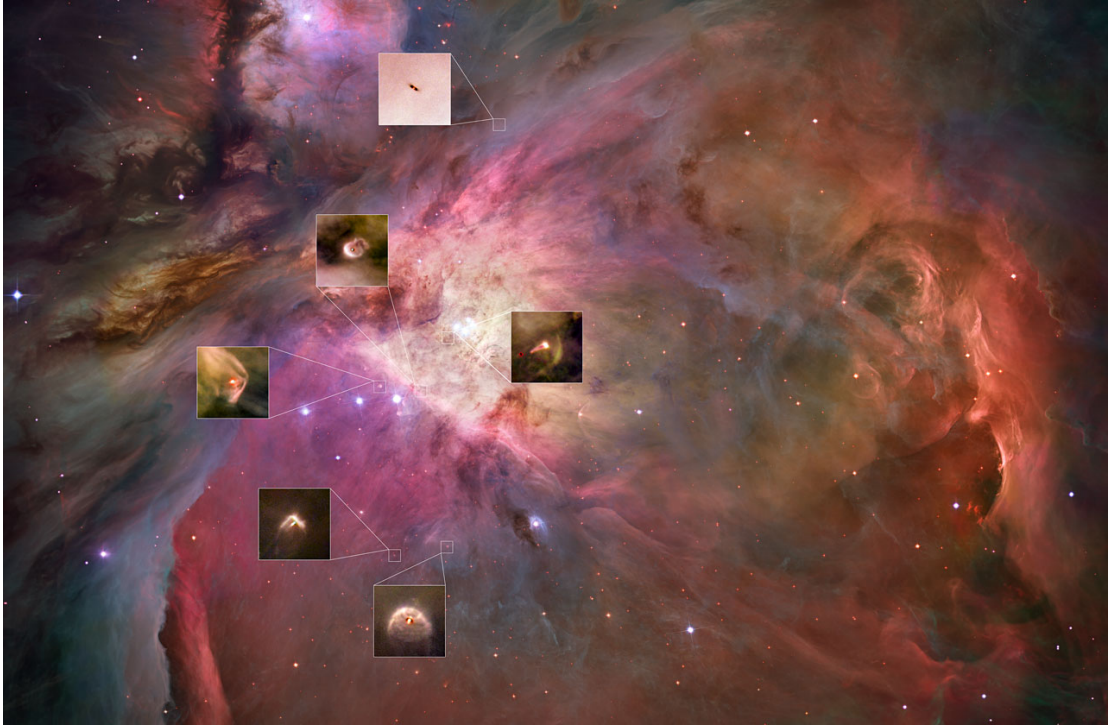


Figure 1.6: Proplyds in the Orion Nebula. The closer a proplyd is to a large, bright star, the more visibly windswept it is. Image courtesy of the Hubble Space Telescope Treasury Program on the Orion Nebula (Robberto et al. (2013))

to dedicate significant time to the ONC, producing an abundance of iconic and awe-inspiring images the cluster and of the disks it hosts (Ricci et al. 2008). These studies have guided many subsequent observations, including many in the radio. Many of the cluster’s protoplanetary disks (or proplyds, as those in the ONC are called) are visibly teardrop-shaped, tailing away from the cluster’s biggest and brightest stars, which are pushing a four parsec-diameter bubble outward at 13 km s^{-1} (Pabst et al. 2019). Images like Fig 1.6, showing disks being pushed away from nearby bright stars, and countless others demonstrate the harsh environment that these young disks exist in. Indeed, the influence of these large stars has already been demonstrated, both in their effect on mass-loss rate and mass distribution. Statistically significant anti-correlations between disk mass and proximity

to the ONC’s central O star, θ^1 Ori C, have been shown using both data from the SMA (Mann & Williams 2009) and ALMA (Mann et al. 2014; Ansdell et al. 2017; Eisner et al. 2018).

Furthermore, both observations (Henney & O’Dell 1999) and modeling (Haworth et al. 2016) characterizing mass-loss rates for these proplyds in the Orion Nebula have found rates of $\dot{M} \approx 10^{-7} - 10^{-5} M_{\odot} \text{ yr}^{-1}$, implying that a typical disk (i.e. one of MMSN-scale, or $\sim 0.01 M_{\odot}$) should be fully dispersed before giant planets could form (Hubickyj et al. 2005) and before they could reach the inferred age of the disk-hosting stars in the ONC of ≈ 2 Myr (Reggiani et al. 2011).

Despite all this, not only do we still see disks, but we still see significant planet-forming potential in the Orion Nebula, potential that is comparable to that of other low-mass SFRs. A full 30% of disks surveyed in the ONC have disks with masses greater than or equal to the MMSN (Mann et al. 2014), falling comfortably between ρ Ophiuchus’ 29% Andrews & Williams (2005) and Taurus’ 37% (Andrews & Williams 2007).

However, since all these surveys are based exclusively on the analysis of dust continuum emission, the comparison is profoundly hamstrung by its reliance on assumptions of gas/dust ratios drawn from the ISM literature. This means that the resulting understanding of the gas masses in these regions is directly proportional to that 100:1 gas/dust ratio, a value that is almost certainly not accurate (as discussed in earlier and in §5). The consequences of this assumption are significant, since a disk’s gas mass directly determines its giant planet forming potential both by setting the amount of raw material available to the forming planet as well as by influencing the environment’s turbulence profile and planets’ migratory patterns within the disk. Furthermore, these continuum surveys cannot reveal

these disks' chemistries and the environmental influences that likely affect them, instead simply assuming solar composition. Together, these assumptions regarding both the total gass mass as well as its composition result in a heavy asterisk accompanying any claims we make about the birth and evolution of protoplanetary disks in high-mass SFRs. To solve this, we must understand the chemical make up of these disks, and for that we need studies of line emission.

Mann et al. (2014) made the first line-emission survey of the Orion proplyds as part of ALMA's Cycle 0 Early Science operation. The survey studied 22 disks in four molecular lines (HCO^+ , HCN, CO, and CS) and $856\mu\text{m}$ continuum, and calculated each disk's dust mass from the continuum emission. Since then, only one of the disks has had its line data analyzed to construct a self-consistent model of temperature and density. Factor et al. (2017) performed an analysis of the radial distribution of one of the disks' gas by modeling emission from the lines to understand the chemical abundance and physical structure of different molecules in the disk. This fitting process was performed on three of the four molecular lines (as CS had insufficient signal to produce meaningful constraints).

In the study, the authors found several unexpected features: their measurement of the disk's HCN abundance was higher than expected (although HCO^+ abundances were consistent with literature values from low-mass SFRs); their mass measurement for the central star was inconsistent with the previously-determined spectral type; and they found a spatially unresolved high-velocity excess emission feature in the $\text{HCO}^+(4-3)$ and $\text{CO}(3-2)$ lines, with a positional offset from the central star. For this emission feature, they found that the source was blue shifted by -6.2 km s^{-1} relative to the systemic velocity, had a position consistent with a $60 \pm 20 \text{ AU}$ Keplerian orbit, and had an inferred H_2 mass of $1.8 - 8 \text{ M}_{\text{Jup}}$. They determined that the excess of emission was caused by a local density and/or temperature

fluctuation in the inner disk, rather than from a jet or cloud contamination. The authors propose that this could be the result of young Mars-sized bodies, collisions between particles trapped in mean motion resonance by a giant planet, magnetic-field-induced zonal flows, or planet formation.

These unexpected results demonstrate the need for further analysis of disks in this survey. The binary system that is the subject of this thesis is drawn from the same survey, representing the second and third ONC proplyds to have their temperature and density profiles characterized.

1.3 d253-1536: A Misaligned Binary System

The subject of this thesis is the system d253-1536, a binary of pre-main sequence stars in the M43 region of the Orion Nebula Cluster. The stars' projected separation is somewhat atypically wide (428 au), and their rotational axes are misaligned (Williams et al. 2014). Each star in the system has its own disk, henceforth called disk A and disk B (east and west, respectively, in all images of the system⁹).

1.3.1 Local Environment & Features

Many previous surveys have studied disks in the famous M42, or Orion Nebula, which lies adjacent to M43, and particularly the Trapezium cluster, a region near M42's brightest star O-star θ^1 Ori C. Mann et al. (2014) found a statistically significant correlation between disk mass and distance from θ^1 Ori C in a study of 70 proplyds (Fig. 1.8), particularly within 0.03 pc of the star, where there is a

⁹The reader will recall that this corresponds to disk A being on the left and disk B on the right of all images, since east and west are inverted in celestial coordinates relative to our familiar geographic ones.

lack of disks more massive than $3 M_{\text{Jup}}$. These disks are also truncated in radial extent, with no disks extending out past 60 AU in this region (Eisner et al. 2018).

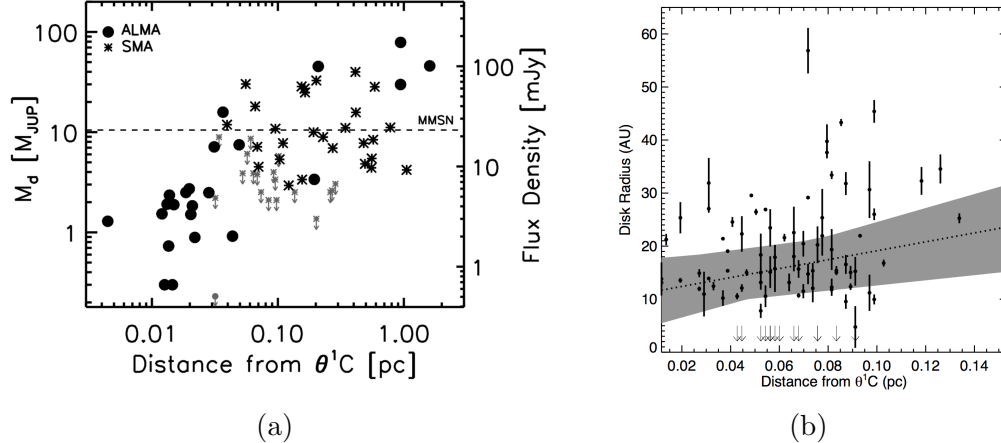


Figure 1.8: *Left:* The masses of 70 ONC proplyds are plotted against their projected distance from the Orion Nebula’s central O-star, θ^1 Ori C, drawn from surveys from ALMA and the SMA (Mann et al. 2014). Grey markers indicate 3σ upper limits for non-detections. The dashed line at $10 M_{\text{Jup}}$ indicates the minimum-mass solar nebula. As is clear from this plot, a statistically-significant correlation was found between disk mass and distance from θ^1 Ori C. *Right:* Radius is also affected by proximity to θ^1 Ori C (Eisner et al. 2018)

However, because of M43’s separation from the Trapezium cluster (it lies ≥ 1 pc to the cluster’s north; see Fig. 1.9), disks in this region do not experience the same levels of photoevaporation. M43 has only one large emitter, NU Ori, which is a triple-star system whose main component is a B-type star. d253-1536 is wrapped in an ionization bow shock, HH 668 A (Fig. 1.10a), about 1" to the system’s west and facing towards NU Ori, but otherwise the system shows no signs of influence from giant stars, whether in photoevaporation or in morphological influences (Mann & Williams 2009).

The system’s larger disk, disk A, has a large jet emanating from it in observations in the optical made with HST (Smith et al. 2005). However, since the jet is not visible in the radio, we make no attempt to discuss, model or explain it.



Figure 1.9: M42 and M43, shown in SDSS coloring, with the locations of d253-1536 (marked with a red circle) and θ^1 Ori C (marked with crosshairs), the heart of the Trapezium cluster. Map created in AladinLite viewer. Because of the large separation between d253-1536 and Trapezium, the disks do not show the same obvious marks of influence from OB stars seen in other disks closer to the heart of M42.

The misalignment of the disks' rotational axes is fairly typical of wide binaries like this one (Williams et al. 2014). The frequency with which these wide binaries present such misalignment indicates that wide binaries likely do not form in large, co-rotating structures, and emphasizes the importance of gas turbulence and interstellar interactions for young stars.

1.3.2 Previous Observations

First observed by Smith et al. (2005) using the Hubble Space Telescope, the authors took interest in what they saw as a binary system containing one star without a disk and one star embedded in a proplyd with a large jet and exhibiting tidal interactions with its companion (Fig 1.10a). Mann & Williams (2009) used

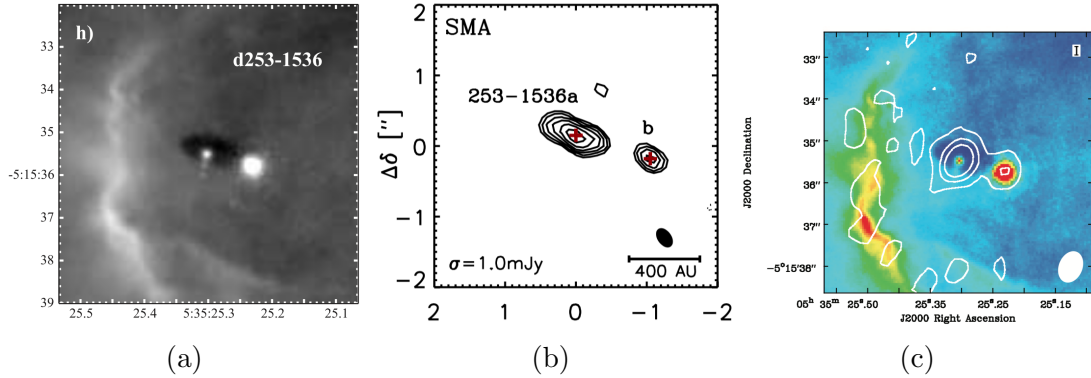


Figure 1.11: Images of V2434 Ori taken from Smith et al. (2005) on HST (Fig. 1.10a), Mann & Williams (2009) with the SMA at $880\text{ }\mu\text{m}$ (Fig. 1.10b), and Ricci et al. (2011) with the EVLA at 7mm (Fig. 1.10c). The ionization front is clearly visible in both the HST and EVLA observations, and the jet from disk A is visible in the HST image.

$880\text{ }\mu\text{m}$ continuum measurements to estimate dust masses of the disks to be $0.066\text{ }M_{\odot}$ and $0.018\text{ }M_{\odot}$, for disks A and B respectively, making d253-1536a the most massive disk measured in the ONC, significantly larger than the cluster's second largest disk ($0.034\text{ }M_{\odot}$) and adding credence to the theory that $\theta^1\text{ Ori C}$ is likely responsible for the truncation of disk masses around the Trapezium cluster. Subsequent detections at 7mm by Ricci et al. (2011) indicated that both disks are hosts to substantial populations of large dust grains (1.10c), although the distributions of grain sizes are different in the two disks. The same study also determined that the spectral type of d253-1536b to be a strongly accreting $0.4\text{ }M_{\odot}\text{ M2}$ star and a $3.5\text{ }M_{\odot}\text{ G2}$ for d253-1536a's host star. This mass ratio of around 9:1 is somewhat atypically high for pre-main sequence binaries (Duchêne & Kraus 2013).

The system was observed in an ALMA survey of 22 proplyds in the ONC by Mann et al. (2014) in four molecular lines: $\text{HCO}^{+}(4-3)$, $\text{HCN}(4-3)$, $\text{CO}(3-2)$, and $\text{CS}(7-6)$ (see Fig. ??). Preliminary fits of the system's kinematics in the

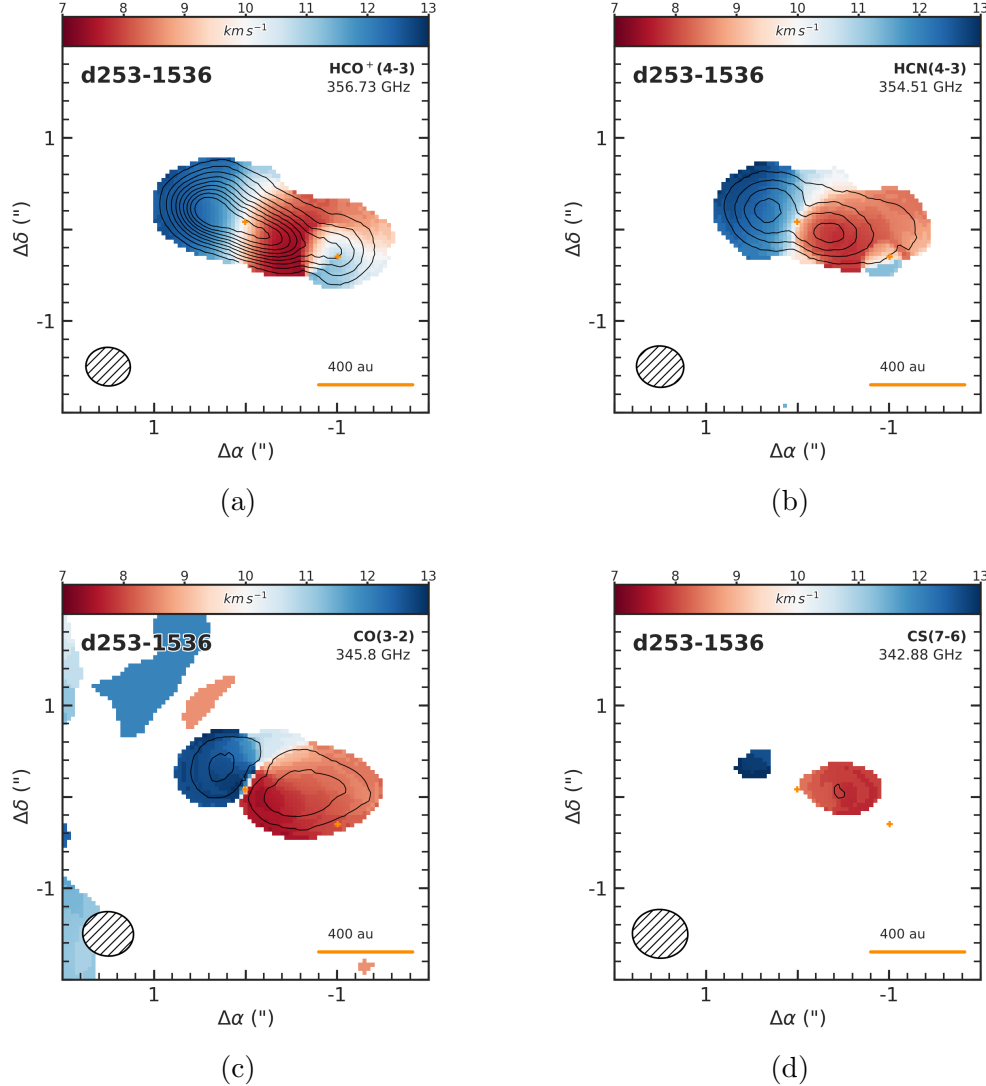


Figure 1.13: Zeroth (contours) and first (colors) moment maps of $HCO^+(4-3)$, $HCN(4-3)$, $CO(3-2)$, and $CS(7-6)$ emission (left to right) in the d253-1536 system, observed with ALMA's Band 7. The moment-zero maps describe the distribution of material in the disks, while moment-one maps give us a sense of the disks' velocity distributions. Moment-zero contours are trace 3, 6, 9... σ flux levels.

$\text{HCO}^+(4-3)$ line were made by Williams et al. (2014). Using continuum observations alone and assuming canonical values for temperature, dust opacity, and gas-to-dust ratio, they found disk masses of 0.074 M_\odot and 0.028 M_\odot for disks A and B, respectively, larger than the previous values. They found an inclination for disk A of $i_A \sim 65^\circ$, but did not resolve disk B and thus were unable to determine its inclination. They found systemic LSRK velocities of 10.55 and 10.85 km s^{-1} for the two disks, which are close enough to be well within the escape velocity that the authors calculated for a pair of disks at their projected separation of 440 AU of 2.5 km s^{-1} , indicating that the binary is bound. This similarity in systemic velocity also indicates that the binary’s orbital plane is likely close to face-on.

1.4 Summary of Contents

With our high resolution observations of gas line emission, we aim to determine the temperature, density, and chemical profiles of two young protoplanetary disks in the d256-1536 system. With these structures in hand, we will examine this disk’s characteristics in the context of previously studied disks in the Taurus and ρ Ophiuchus star forming regions, as well as comparing it to the disk studied by Factor et al. (2017). Observations and data reduction are described in §2. In §3, data and basic analysis are presented. Descriptions of modeling and fitting techniques are discussed in §4, and in §5, best-fit parameters are discussed and contextualized.

Chapter 2

Observations

The data presented in this thesis are part of an ALMA survey of Orion proplyds in Orion (project 2011.0.00028.S); data collection and analysis methods of the continuum results are presented in Mann et al. (2014). The observations were taken on 2012 October 24, using ALMA’s Band 7 receivers. Four spectral windows of width 1.875 GHz were arranged to cover the rest frequencies of the HCO^+ (4-3), HCN(4-3), CO(3-2), and CS(7-6) transitions (356.734 GHz, 354.505 GHz, 345.796 GHz, and 342.883 GHz, respectively). Each window was split into 3840 channels with a width of 488.28 kHz, yielding a velocity resolution of 0.42 km s^{-1} . Since this was part of a Cycle 0 Early Science project, the survey used only 22 of ALMA’s 50 12 meter dishes in a hybrid configuration, with physical (non-projected) baselines ranging from 21.2 to 384.2 meters. This configuration yields a maximum angular scale of $8''$, angular resolution of $0''.5$, and beam FWHM of $15''$. At a distance of 389 ± 7.97 (Gaia Collaboration 2016; Gaia Collaboration et al. 2018)¹, maximum angular scales and angular resolution correspond to 3,112 AU and 194 AU, respectively. The observation’s pointing center was (05:35:25.30, -05:15:35.50). Each disk’s precise position was fit for (see §4), and are given in Table 2.1.

These data, from Field 4 of Mann et al. (2014) represent 13.6 minutes of on-

¹This measurement is nearer than the previous literature value of 414 pc adopted by (Factor et al. 2017).

Table 2.1: Disk Positions

Source	RA	Dec
d253-1536a (disk A)	05 : 35 : 25.3002	-05 : 15 : 34.418
d253-1536b (disk B)	05 : 35 : 24.2940	-05 : 15 : 35.800

source time. This duration was split into six 136 second observations, spaced out over 7.5 hours to ensure adequate *uv* coverage, yielding an RMS of 7 mJy beam⁻¹ in the line data. With natural weighting, the resulting synthesized beam has dimensions of 0."57×0."51 with a position angle of 85°. Precipitable water vapor in the atmosphere was stable at 0.7 mm.

The data were calibrated by ALMA staff using standard procedures in the Common Astronomy Software Applications, or CASA (McMullin et al. 2007). The antenna-based complex gains and bandpass response of the system were calibrated using observations of the quasars J0607-085 and J0522-364 respectively. The absolute flux calibration was determined from observations of Callisto, using a model drawn from Butler (2012). Absolute flux calibration is estimated to be accurate to within ∼10% (Mann et al. 2014).

The velocity reference frame was converted from CASA’s standard topocentric frame to LSRK (kinematic local standard of rest) using the CASA task `cvel`. Next, continuum emission was subtracted from the data in the uv plane using the CASA task `contsub`. Visibilities were imaged with standard inversion, deconvolution, and restoration procedures from the Multichannel Image Reconstruction Image Analysis and Display, or MIRIAD, package (Sault et al. 1995).

Chapter 3

Results

Spatially and spectrally resolved line emission was detected for CO (3-2), HCO⁺ (4-3), HCN (4-3), and CS (7-6) across around 50 channels with velocity resolution of 0.42 km s⁻¹. Here we present a discussion of these data, including line-emission statistics, diagnostic plots, and a consideration of the cloud contamination present in the observations.

3.1 Cloud Contamination

Cloud contamination occurs when emission from gas clouds along the observation's line of sight is detected. This is typically not a significant issue for observations of protoplanetary disks in low-mass star forming regions (SFRs), but since the Orion Nebula has a significantly higher gas density than those low-mass SFRs, cloud contamination becomes problematic. This is particularly evident in the CO line, thanks to its low critical density and relatively high abundance in the background clouds, which allows it to excite and emit more readily than other molecules. As a result of higher critical densities and lower abundances, cloud contamination is less significant, but still present, in the other lines. It is crucial to manage and minimize the effects of this contamination before modeling so that our fitting algorithms do not try to model the cloud emission.

Luckily, there exist ways to minimize the effects of cloud contamination. An

obvious way to do this would be to simply crop out the contaminated regions; however, since we model in the visibility domain (a Fourier transform away from the image domain), cloud contamination cannot be separated by physical location as it could in the image domain. Instead, we take advantage of the fact that the contaminating clouds tend to be very large relative to a proplyds and that, as discussed in §1, interferometers have the ability to filter by length scale. Using these two features, we may exclude a selection of the shortest baselines used in our data, effectively shrinking the largest angular scales to which our observations are sensitive. This, in turn, significantly reduces the effects of the cloud emission, since those short baselines that are recording the noise are also too short to be recording meaningful information about the disk¹.

To characterize the cloud contamination in our images, we iteratively remove more and more of the shortest baselines from our data and measure the resulting RMS noise of an off-source area at each step. Were there no cloud contamination, this plot of RMS vs. min-baseline would trend upwards (following the fact that noise is typically proportional to the inverse square root of amount of data). However, we can recognize the signature of cloud contamination if we find unexpectedly high noise at low baselines that falls off at longer ones. This indicates that the optimal value to use as our minimum baseline length would be the inflection point at which the cloud contamination’s contribution (decreasing with baseline length) gives way to the normal losses that come with decreasing signal (increasing with baseline length). The results of making such plots are shown in Fig. 3.1.

¹This can be shown with a quick calculation of the angular resolution of the short baselines. We can easily consider the angular resolution of a $40\text{ k}\lambda$ baseline: $\theta = \lambda/D = 1/(40\,000)$ radians $\gtrapprox 5''$. At Orion’s distance of 389 pc, this corresponds to ~ 2000 au, larger than the $\sim 2''$ (< 800 au) that our disks span.

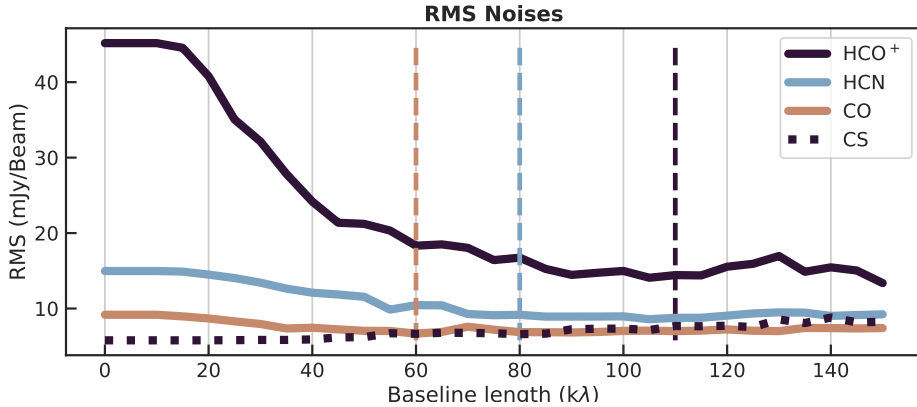


Figure 3.1: Noise profiles as a function of minimum baseline length for the four molecular lines in our dataset. Dashed lines represent optimal cut locations, at the minimum where cloud contamination is noise that is introduced from removing data is not yet too large. Since CS (dotted line) has no cloud contamination, we do not remove any baselines from it. Quantitative results from this process are summarized in Table 3.1.

From these plots, we find that excluding baselines less than 110 k λ , 80 k λ , and 60 k λ for HCO⁺, HCN, and CO, respectively, yielded optimum results. Since emission from the CS line already has a very low SNR and a higher critical density than the clouds can easily access, it showed minimal contamination and thus excluding baselines did not improve the observations. Images of the data with and without the cuts implemented are presented in 3.2.

3.2 Line Emission Statistics

Integrated line flux was measured using the Miriad task `cgcurs` to measure the total flux in a zeroth moment map over the region enclosed by the 3 σ contour. Due to the disks' overlap and interaction with one another, defining the disks' boundaries (and consequently where to place the bounding box for their flux measurements) is not entirely clear. This introduces a significant source of uncertainty in the calculation of total disk flux, as noted in Williams et al.

Table 3.1: Integrated Flux Measurements with Baseline Cuts

Molecular Line	Baselines Included	Max Angular Scale (")	Integrated Line Flux (Jy km s^{-1})	
			Disk A	Disk B
CO (3-2)	All	8.4	*	*
CO (3-2)	$> 60k\lambda$	3.4	2.58 ± 0.47	1.85 ± 0.39
HCN (4-3)	All	8.2	0.80 ± 0.07	0.26 ± 0.08
HCN (4-3)	$> 80k\lambda$	2.6	0.69 ± 0.05	0.17 ± 0.08
HCO ⁺ (4-3)	All	8.2	5.79 ± 0.49	2.29 ± 0.56
HCO ⁺ (4-3)	$> 110k\lambda$	1.9	4.15 ± 0.31	0.80 ± 0.22
CS (7-6)	All	8.5	0.024 ± 0.02	[no detection]

* Integrated line intensity was not calculated for CO(3-2) before the baseline cuts, as the data were too contaminated to give meaningful results.

(2014), which they estimate to be around 30%, although the distribution of this uncertainty is likely skewed towards overestimation due to the excess of emission contained within the 3σ contour. The results of these measurements are shown in Table 3.1. From these values, we may estimate the disks' gas masses.

Assuming optically thin emission and Local Thermodynamic Equilibrium (LTE), the line-emitting gas mass, M_{gas} is given by:

$$M_{\text{gas}} = \frac{4\pi}{h\nu_0} \frac{Fmd^2}{A_{ul}X_u}, \quad (3.1)$$

where F is the integrated line flux, m is the mass of the emitting gas molecule, d is the distance to the source, h is the Planck constant, ν_0 is the molecular line's rest frequency, A_{ul} is the Einstein coefficient for the $(u - l)$ transition, and X_u is the ratio of the number of molecules in the upper state to the total number of molecules, defined by

Table 3.2: Values Used in Gas Mass Calculation (for HCO⁺(4-3))

Parameter	Value	Description	Source
F ($\frac{\text{erg Hz}}{\text{cm}^2 \text{s Hz}}$)	7.12×10^{-12}	Integrated line flux	1
ν_0 (GHz)	356.73	Rest frequency	2
J	4	Quantum number of upper level	
A ₄₋₃ (s ⁻¹)	3.63×10^{-3}	Einsten A coefficient	2
B ₀ (cm ⁻¹)	1.488	Rotational constant	1
T _{ex}	17	Excitation Temperature	3
d (pc)	389	Distance	4
m (g)	$29 \times m_{\text{proton}}$	Mass of molecule	2

¹ Calculated with MIRIAD task `cgcurs`² Schöier et al. (2005)³ Factor et al. (2017)⁴ Gaia Collaboration et al. (2018)

$$X_u = \frac{N_u}{N_{\text{tot}}} = (2J_u + 1) \frac{\exp[-B_0 J_u (J_u + 1) hc/kT_{\text{ex}}]}{kT_{\text{ex}}/hcB_0}. \quad (3.2)$$

The values used for this measurement and descriptions of them are given in Table 3.2.

We now turn to visualizing our data. Since line emission has a third (spectral) dimension, visualizing it presents a unique opportunity and challenge. Moment maps offer us an intuitive way to flatten the three-dimensional data-cube (in α, δ, v) into two dimensions. Moment 0 maps integrate flux along the velocity axis as a function of position, providing insight into structures of emission intensity in the disk's morphology (and essentially sacrificing the data's spectral information), while moment 1 maps, a velocity-weighted intensity integration across position, tell us about a source's velocity gradients. Fig. 3.2 show zeroth- and first-moment maps, respectively, of emission from the CO, HCO⁺, and HCN lines, with and

without short baselines (as defined in Table 3.1) removed (right and left, respectively).

With moment maps, we flatten through the velocity axis, but we may also flatten through the spatial dimensions as well using a position-velocity diagram (PVD). PVDs allow us to directly observe the velocity dispersion along a given axis in the image; usually this is a disk's major axis. In Fig. 3.3, we show a PVD of disk A's HCO⁺ emission. In it, we see some noticeable asymmetry, both in terms of centroid intensity and in the extra feature at the eastern side of the map, which is likely the tail of disk B.

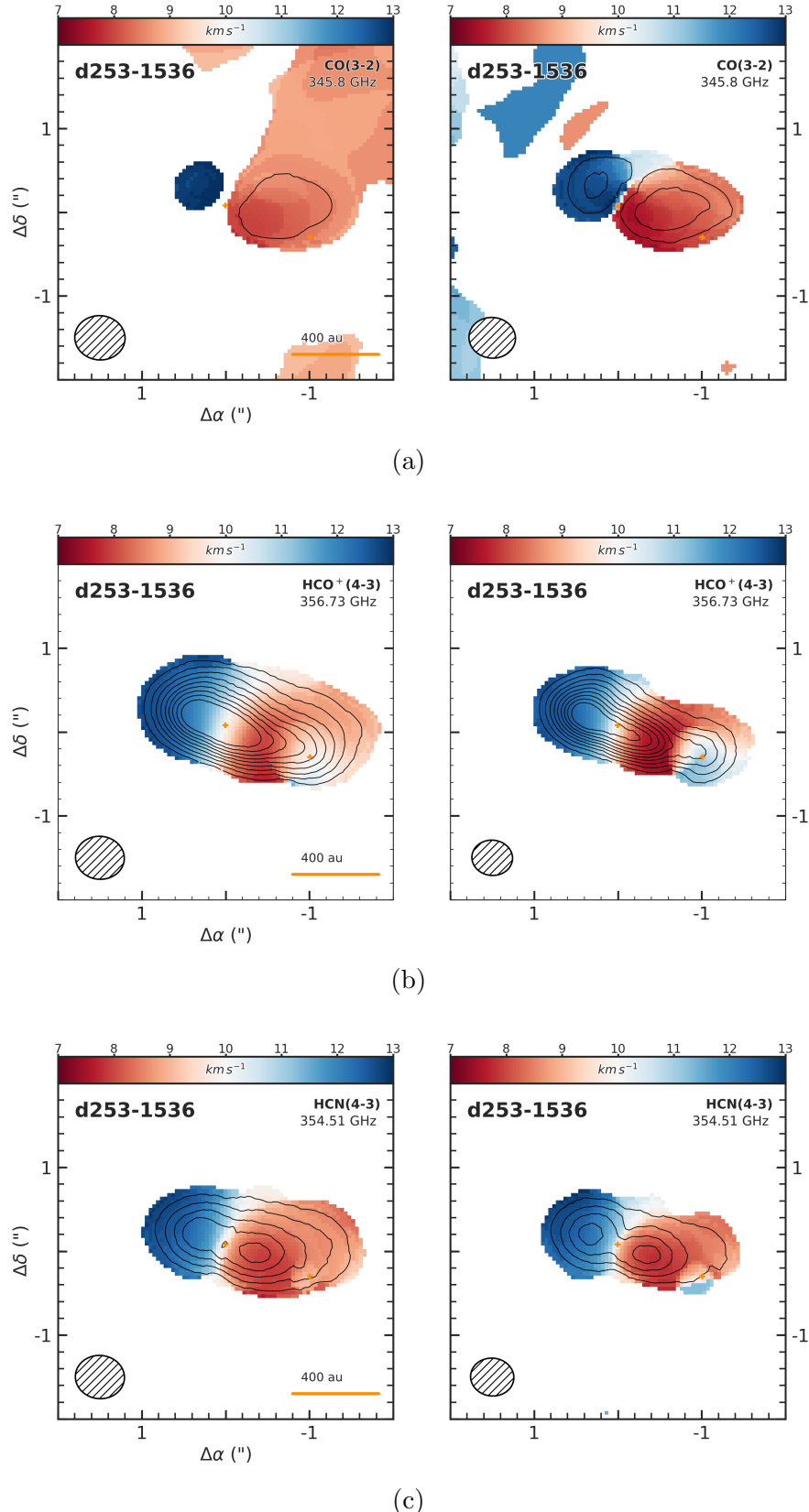


Figure 3.2: Zeroth (contour) and first (color) moment maps of emission from CO, HCO⁺, and HCN are presented. For each pair, the data is shown without (left) and with (right) baseline cuts implemented according to values given in in

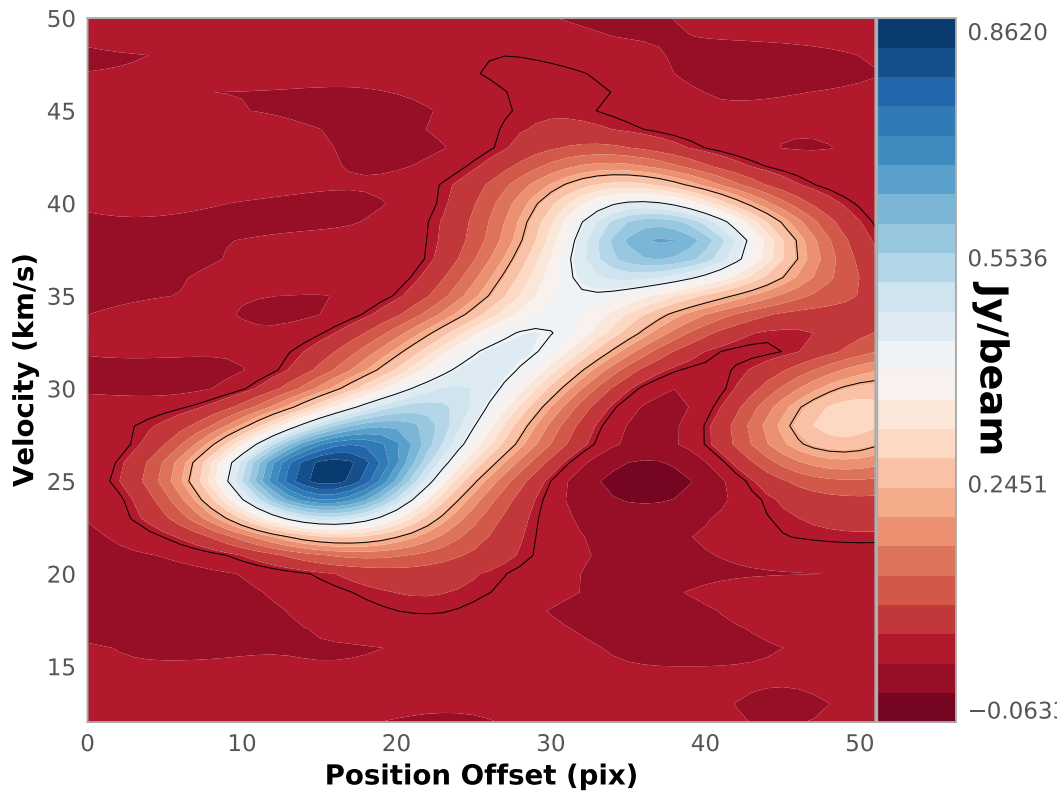


Figure 3.3: A PV diagram of disk A's HCO^+ emission, where the x-axis is centered on the disk's position and offset is measured along the disk's position angle. Some asymmetries are readily noticeable, and are likely caused by disk B and excess emission from interactions between the two disks.

Chapter 4

Analysis

By modeling spatially and spectrally resolved observations of protoplanetary disks, we can measure their chemical and physical characteristics. To model the system, we generate a synthetic image of what a disk with known characteristics (like disk radius, mass, chemical abundances, and so on) would look like at a certain distance, inclination, and position angle relative to us. We can then turn that synthetic image into a synthetic visibility set, and then compare those visibilities to our observations. By iterating this process and varying the value of those input parameters, we are able to generate many models with different parameter combinations, evaluate how well each resulting model disk matches our observations, and find which values best describe our disks.

In §4.1, we describe the basic equations and computational processes that generate the model disks. In §4.2, we describe how, once models are made, we move through high-dimensional parameter space to identify regions of best-fit. Finally, in §4.3, we present the results of our fitting procedures.

4.1 Gas Model

In this work, we use a gas disk model originally developed by Rosenfeld et al. (2012, 2013) and translated from IDL to Python by Flaherty et al. (2015). The

code assumes local thermal equilibrium¹ (LTE) and hydrostatic equilibrium. The code draws on temperature and surface density profiles provided by the user to calculate a vertical density structure, and calculates the model disk’s velocity field based on the stellar mass. It then performs radiative transfer on the resulting structure to create a sky-projected image of the model disk, taking into account thermal and turbulent line broadening. The assumption of LTE allows the code to run quickly enough for a Markov Chain Monte Carlo routine to generate many models on a reasonable timescale, as described in §4.2.2.

4.1.1 Establishing Physical Profiles

A circumstellar disk can be characterized by three major profiles: its radial and vertical temperature structures, its radial and vertical density structures, and its velocity field. Generating a model disk is a matter of defining these three functions.

For the disk’s temperature profile, our code uses the parametrization of disk temperature structure first laid out by Dartois et al. (2003), where the disk’s temperature is given by,

$$T_{\text{gas}}(r, z) = \begin{cases} T_a + (T_m - T_a) \left[\cos \frac{\pi z}{2z_q} \right]^{2\delta} & \text{if } z > z_q \\ T_a & \text{if } z \leq z_q(r). \end{cases} \quad (4.1)$$

δ , a tunable exponent controlling the rate of the disk’s vertical temperature decay, is set to 1 as in Factor et al. (2017), though it can take on values between

¹This may or may not be a valid assumption in protoplanetary disks, but Pavlyuchenkov et al. (2007) showed that it was appropriate for CO.

1-2 (Dartois et al. 2003). The atmospheric temperature and mid-plane temperatures are given by $T_a = T_{\text{atm},150}(r/150 \text{ au})^q$ and $T_m = T_{\text{mid},150}(r/150 \text{ au})^q$, where q is typically negative and controls the disk's radial temperature decay. Since T_m is smaller than T_a , the second term of the low-scale height temperature function is negative, so the sinusoid effectively implements a decreasingly-negative contribution to the temperature with height above midplane. The disk's scale height, controlled by z_q , is assumed to be radially increasing, as described by a power law, $z_q(r) = z_{q,150}(r/150 \text{ au})^{1.3}$.

The disk's velocity field is assumed to be Keplerian with slight corrections for gas pressure support and the addition of a vertical dependence. The assumption of Keplerian velocities is generally valid in the case that $M_{\text{disk}} \ll M_{\star}$, which continuum observations of the system have shown to be the case for these disks. With these corrections added, the model disk's velocity field is given by

$$\frac{v_{\phi}^2}{r} = \frac{GM_{\star}r}{(r+z)^{3/2}} + \frac{1}{\rho_{\text{gas}}} \frac{\partial P_{\text{gas}}}{\partial r}; \quad v_r = v_z = 0. \quad (4.2)$$

(4.3)

The final structure we define is the disk's gas density profile. By assuming hydrostatic equilibrium, we may relate the disk's gas density and temperature profiles as

$$-\frac{\partial \ln \rho_{\text{gas}}}{\partial z} = \frac{\partial \ln T_{\text{gas}}}{\partial z} + \frac{1}{c_s^2} \left[\frac{GMz}{(r^2+z^2)^{3/2}} \right]. \quad (4.4)$$

Here c_s is the local sound speed, given by $c_s^2 = \frac{k_B T_{\text{gas}}}{\mu m_H}$, T_{gas} is the temperature

profile given above, m_H the mass of hydrogen, and μ is the mean molecular weight of the gas, set here at 2.37 to reflect the gas's 80% H₂ composition. We may solve this equation by integration, giving us the disk's density profile $\rho(r, z)$.

The model's surface density profile is drawn from Hartmann et al. (1998), in which they expanded on the work of Lynden-Bell & Pringle (1974) to show that the structure of an isolated disk with viscosity given by $\nu \propto R^\gamma$ is well-described by

$$\Sigma_{\text{gas}}(r) = \frac{M_{\text{gas}}(2 - \gamma)}{2\pi R_c^2} \left(\frac{r}{R_c}\right)^{-\gamma} \exp\left[-\left(\frac{r}{R_c}\right)^{2-\gamma}\right], \quad (4.5)$$

where R_c is the radial extent of the gas disk, γ is a power law index, and M_{gas} is the total gas mass. This form allows the disk to behave as a power law radially until R_c , at which point it turns over into exponential decay. Hughes et al. (2008) showed that exponentially tapering the disk's outer radius, rather than sharply cutting it, provides the best agreement between gas and disk outer radii. We approximate $M_{\text{gas}} = M_{\text{disk}}$, since at this early stage in the disk's development, the gas is by far the majority element of the disk's mass total (although, as discussed in §1, this assumption has come under scrutiny in recent years).

Modifications are made to this density profile in two cases. At sufficiently low temperatures, molecules will freeze out of the gas phase. The mid-plane of the disk is sufficiently cold to prompt this behavior. We simulate this behavior by dropping the gas density by a factor of 10^{-18} wherever the temperature falls below some characteristic freeze-out temperature, T_{FO} , a temperature which is molecule-specific. Conversely, at the disk's upper surface, photodissociation by stellar and interstellar radiation dominates, so we implement a decrease in density wherever

Table 4.1: Molecule-specific values

Parameter	Description	Fixed Value(s)		
		CO,	HCO ⁺	HCN
T _{FO} (K)	Molecular freeze-out temperature	19	60	
σ _{Max} (cm ⁻²)	Column density upper limit	1.3 × 10 ³⁰	9.5 × 10 ²¹	

* Values drawn from Factor et al. (2017)

the hydrogen column density at the disk's surface falls below a characteristic value. We use values drawn from Factor et al. (2017) for these parameters, presented in Table 4.1.

4.1.2 Generating a Model Image

Having now established our model disk's physical structure through temperature, density, and velocity profiles, flux contributions through the disk are calculated. To do so, we find specific intensity by integrating the equation of radiative transfer:

$$I_\nu = \int_0^\infty K_\nu(s) S_\nu(s) e^{-\tau_\nu(s)} ds, \quad (4.6)$$

where $K_\nu(s)$ is the absorption coefficient, $\tau_\nu(s)$ is the optical depth and is defined as $\tau_\nu(s) = \int_0^s K_\nu(s')ds'$, and $S_\nu(s)$ is the source function. Since disks emit as blackbodies, the Planck function, $B_\nu(T)$, is used as the source function. Line broadening, a function of temperature and disk turbulence, is added, and the resulting flux is Doppler shifted to account for the disk's user-specified systemic velocity. Finally, the image is scaled, shifted, and rotated to account for the source's distance (d), angular offset from the center of the image ($Δα$ and $Δδ$),

and position angle and inclination (PA and i) relative to our viewing direction.

Since the model disk is fully defined at every point in both physical and velocity space, we may set the spatial and spectral resolution to ensure that it is sampled well compared to the resolution of the data. We set our spectral resolution to match that of our observation, while we let the spatial resolution be $\sim 1/10$ the size of the synthesized beam. This resolution is high enough to avoid sampling artifacts when we simulate interferometric observations of the image. We then use the Miriad task `uvmodel` to generate visibilities from the model image, sampled in the same uv tracks as our observation. The χ^2 statistic is then used as a goodness-of-fit metric to compare the data and model in the visibility domain. We make this calculation in the visibility domain, rather than the image domain, so that the resulting χ^2 value is not influenced by artifacts generated in the imaging process.

In summary, we can generate a model disk by calculating its physical structures (in radial temperatures, densities, and velocities), then draws on radiative transfer to calculate the flux contributions from the disk. That flux is sky-projected to match the observed source's orientation, and the resulting image is then transformed from the image domain to the visibility domain and the quality of its fit is evaluated.

4.2 Exploring Parameter Space

Now that we have the tools available to generate synthetic images that are tunable across a large number of parameters, we must decide how best to move through that large parameter space to find a best-fit region. To do so, we use two methods.

4.2.1 Grid Search

The first, and perhaps most intuitive, way to move through this parameter space is using a simple grid search. A grid search involves manually assembling lists of values to try for each parameter and then generating models and calculating the resulting χ^2 value for every possible combination of parameters in those lists. A best-fit value is recovered by simply finding the point in that n -dimensional grid that yielded the best χ^2 , and then either calling that position in parameter space a best-fit location or then defining a finer grid around that point and repeating the process until an acceptable resolution has been reached. Benefits of grid search include its relatively straightforward nature (and, consequentially, the relative simplicity of implementing it) and its usefulness as a diagnostic tool, since very specific regions of parameter space may be sampled with the manual entry of positions to test. However, grid searches are inefficient since they spend a significant amount of time sampling regions of parameter space that are not near the global minimum. This inefficiency leaves room for improvement.

We used grid search to locate the disks in (α, δ, v) space. All other parameters were fixed at best-guessed values, then grids were run with resolutions sufficiently fine to meet the observations' spatial and spectral resolution. Grids for the disks' systemic velocities were centered at values found in Williams et al. (2014), while $\Delta\alpha$ and $\Delta\delta$ offsets were first approximated using the MIRIAD task `uvfit` to fit a Gaussian to each disk. The resulting centroids were used to center the grids for refinement.

4.2.2 Markov Chain Monte Carlo

Markov Chain Monte Carlo (MCMC) algorithms present a way to sample the probability distribution of a high-dimensional parameter space (much like a grid search), but offers an improvement over grid search by yielding the posterior probability distribution of each point, which allows us to characterize the uncertainty associated with each best-fit value with error bars. We use an affine-invariant formulation of the MCMC algorithm described by Goodman & Weare (2010) and implemented in the Python package `emcee` by Foreman-Mackey et al. (2013).

MCMC routines sample the probability distribution of a given n -dimensional parameter space by deploying an army of “walkers.” Each walker begins at some initial position, evaluates the χ^2 value of that point, and then proposes moving to a new position in parameter space according to a Gaussian probability distribution centered at the current point and decaying with distance (so that nearer points are preferentially, but not necessarily, selected). The χ^2 value of this new position - or “step” - is then evaluated, and is either accepted (the walker moves to that position) or rejected (the walker remains where it is and repeats the new-step proposal process) with probability $p = \exp [(\chi_{\text{current}}^2 - \chi_{\text{new}}^2)/2]$.² This function indicates that if the proposed step yields a better fit (a lower χ^2 value) than the current position, $p > 1$ and the step is accepted. However, if proposed step results in a worse fit, there is still a non-zero chance that the step is accepted, proportional to how much worse it is. Goodman & Weare (2010) show that a walker’s desire to remain in near a certain position is proportional to that position’s local probability density, meaning that we may infer uncertainties in our fits from the density of walker steps taken in a region.

²In practice, we take the natural log of both sides of this equation, such that the quantity we are really evaluating is $\text{lnprob} = \Delta\chi^2/2$.

We may introduce boundaries to the parameter space explored by our walkers using “priors.” These priors are manually set, and allow us to restrict the walkers’ motions from entering regions that we know a priori to be implausible fits. Justifications for these constraints are either physical (e.g. a disk should not have a negative radius) or observed (e.g. both disks’ radii are clearly far less than 1000 AU). These priors may be either uniform, with hard cuts at their bounds (and returning $\text{lnprob} = -\infty$), or Gaussian, with preferential treatment given to walkers closer to the Gaussian centroid (a known value). For this work, we implement a Gaussian prior on each disk’s position angle in order to guide the search towards the values reported in Williams et al. (2014) but still allow it the flexibility to self-correct if necessary. This prior takes the form of a contribution to the log likelihood function, such that:

$$\text{lnprob} = -\chi/2 - \ln \frac{1}{\sqrt{2\pi\sigma_{PA}^2}} \exp\left(\frac{\text{PA}^2}{2\sigma_{PA}^2}\right) \quad (4.7)$$

for each disk’s position angle, where σ_{PA} is the position angle uncertainty given by Williams et al. (2014).

We may visualize the results of the walkers’ journeys using corner plots. Corner plots allow high-dimensional space to be visualized in two dimensions by taking slices across each pair of axes and showing the density of samples drawn in that slice. In each of these slices, a perfectly certain fit would appear as a very tight, point-like Gaussian - the sample density around the best fit would be extremely high and low everywhere else, as the walkers quickly converged and remained on that best fit point - while conversely, higher uncertainties are shown by a wide spread of samples around the central point. Degeneracies between parameters can

be seen as streaks in these corner plots, showing that a change in one parameter produces a change in the other. Corner plots for the MCMC fitting of $\text{HCO}^+(4-3)$ emission (see Fig. 4.1) show good convergence, with little to no degeneracies between parameters.



Figure 4.1: Cornerplots of our $\text{HCO}^+(4-3)$ fitting show fairly good convergence.

4.3 Fitting Procedure

Fitting of the data began with the analysis and partial removal of cloud contamination, resulting in the removal of baselines below a characteristic length for each line as discussed in §3. With the data as clean as possible, position ($\Delta\alpha, \Delta\delta$) and velocity (v_{sys}) offsets were fit with a grid search. Offset fitting was executed only on the HCO⁺line, thanks to the line's minimal contamination and high signal strength. With these values established, they were treated as fixed parameters for the remainder of the fitting process.

Table 4.2: Fixed Parameter Values

Parameter	Description	Ref.	Fixed Value(s)	
			Disk A	Disk B
$\Delta\alpha$ ('')	RA offset from image center	0	0.0002	-1.006
$\Delta\delta$ ('')	Dec offset from image center	0	0.082	-0.3
v_{sys} (km s ⁻¹)	Systemic velocity	0	10.00	10.75
i (°)	Inclination	1	65	45
M_\star (M_\odot)	Stellar mass	1	3.5	0.4
Log M_{disk} (M_\odot)	Disk gas mass [*]	1	-1.11	-1.55
v_{turb} (km s ⁻¹)	Turbulence velocity	2		0.081
d (pc)	Distance	3		389
R_c (au)	Critical radius	1		100
γ	Radial density power law index	4		1
z_q (au)	Disk scale height at 150 AU	5		29
T_{mid} (K)	Midplane temp. at 150 AU	6		19

^{*} M_{disk} is fixed in our fitting of HCO⁺and HCN, and varied for CO.

⁰ Grid-search and/or elliptical fitting, as described in §4.2.1

¹ Williams et al. (2014)

² Flaherty et al. (2015)

³ Gaia Collaboration et al. (2018)

⁴ Andrews et al. (2009)

⁵ Factor et al. (2017)

⁶ Qi et al. (2011)

Table 4.3: Fit Parameter Values

Parameter	Description	Prior
$\log X_{\text{mol}}$	Molecular abundance, relative to H_2 ^a	Log Uniform
q	Radial temperature power law index	Uniform
PA ($^\circ$)	Position Angle ^b	Gaussian
$T_{\text{atms}} \text{ (K)}$	Atmospheric temperature at 150 AU	Uniform
$\log M_{\text{Disk}} \text{ (M}_\odot)$	Disk gas mass [*]	Log Uniform

^a For the CO line, X_{mol} is fixed at the literature value of 10^{-4} .

^b In our CO fit, disk B's position angle is fixed at the best-fit value from the HCO^+ fits.

^{*} For HCO^+ and HCN, disk mass was fixed at values from Williams et al. (2014).

Table 4.2 presents a list of parameters, including $\Delta\alpha$, $\Delta\delta$, and v_{sys} , which were left fixed throughout the MCMC runs. Since we are only modeling one line at a time, we are unable to constrain the vertical temperature structure and so fix T_{mid} and z_q . The selection of T_{mid} was made following Factor et al. (2017) to reflect the “CO snow line” shown by Qi et al. (2011)³, while the value of z_q was chosen, again following Factor et al. (2017), to be roughly double the disks’ scale heights, as shown in Rosenfeld et al. (2013). Since HCO^+ is optically thin, temperature and density are degenerate, so γ is set at 1 following Andrews et al. (2009), who showed this to be a reasonable value for disks in ρ Ophiuchus. Since our observations do not have enough spectral resolution to constrain the observations’ turbulent linewidth, we fix v_{turb} at around 1% of the sound speed, per Flaherty et al. (2015).

When fitting CO, we fix its abundance at the canonical value of 10^{-4} and instead fit for disk mass. Conversely, in our fits of HCO^+ and HCN emission, we fix M_{disk} at values drawn from Williams et al. (2014), which they infer from continuum flux measurements (and relying on the 100:1 gas/dust ratio discussed in §1). The remaining parameters are fit for using MCMC. We implement priors

³Although their measurements were made for sources in a different environment, the value gives us a reasonable starting point for our fits.

on each parameter, reported in Table 4.3. The results from the MCMC runs are presented below. To facilitate easier reading, accompanying figures are found at the end of the chapter.

4.3.1 HCO⁺(4-3) Fit

We began by fitting the HCO⁺(4-3) line, using the MCMC methods explained above. Best fit and median values with 1σ uncertainties are given in Table 4.4. Fit posteriors, showing how well the MCMC walkers constrained each parameter, and moment maps of the data, model, and residuals are given in 4.3 and 4.6, respectively.

We see from the corner plots that, in general, the fits are quite well constrained. Uncertainties surrounding disk B's outer radius lead to some degeneracies, but overall this fit seems to be well managed. Inspection of the moment maps of the HCO⁺ data, best-fit model, and residuals (Fig. 4.6) show that, while the model seems to reproduce the data's morphological structure fairly well, fluxes are systematically low, leaving significant residuals.

Table 4.4: MCMC Fitting Results (HCO⁺)

Parameter	Disk A		Disk B	
	Median	Best Fit	Median	Best Fit
R _{out} (au)	339 ⁺⁸ ₋₇	341	246 ⁺¹⁰¹ ₋₁₀₀	148
T _{atms} (K)	210 ⁺¹¹⁰ ₋₅₀	200	190 ⁺¹²⁰ ₋₁₂₀	180
X _{HCO⁺}	-8.4 ^{+0.3} _{-0.3}	-8.2	-10.3 ^{+0.6} _{-0.3}	-9.8
PA (°)	69.9 ^{+1.5} _{-1.2}	69.5	129 ⁺¹² ₋₁₄	126
q	0.8 ^{+0.3} _{-0.4}	0.7	[-0.5]	[-0.5]
lnprob			-28402	

* Values in [brackets] were fixed for this run.

4.3.2 HCN(4-3) Fit

Next we model HCN, using the same methods as for HCO^+ . As before, best fit and median values with 1σ uncertainties are given in Table 4.6, posterior distribution functions are shown in Fig. 4.4, and data/model/residual moment maps are shown in Fig. 4.6.

In the channel maps, we see that the fit is generally good, leaving fairly minimal residuals behind. The residuals do, however, highlight a stream of flux connecting the two disks, particularly at velocities around $9.4 - 10.2 \text{ km s}^{-1}$ that our model is unable to fit. This stream is most visible in the HCN line, compared to the HCO^+ and CO maps.

For both disks, the posterior distribution of fits to outer radius is bimodal. This likely is a result of the MCMC walkers struggling to make sense of the above-mentioned bridge between the disks. This is particularly the case with disk B, where the walkers are distributed around 100 au and around 350 au. As a test, we can remove all steps in the MCMC chain where disk B's outer radius exceeds 250 au (which is somewhere in the middle of the bimodality in the parameter's posterior distribution, but is still appreciably higher than the HCO^+ fit value of ~ 150 au). Implementing these cuts brings HCN's best-fit values for disk B's radius and temperature into much closer agreement with HCO^+ (120 au K compared to 148 au and 170 K compared to 180 K for outer radius and temperature in HCN and HCO^+ , respectively). Table ?? presents the updated fit statistics with the disk B radius cut implemented. As a visual check on whether this yields a better fit, Fig 4.2 shows HCN's first moment map with both best-fit disk B radii (380 au and 120 au) plotted.

Otherwise, the fit's posteriors are widely unimodal; they are also less tightly

constrained than those from the HCO⁺fits, yielding a lower likelihood. There are no particularly noticeable degeneracies between parameters.

Table 4.5: MCMC Fitting Results (HCN)

Parameter	Disk A		Disk B	
	Median	Best Fit	Median	Best Fit
R _{out} (au)	420 ⁺¹⁸⁰ ₋₁₀₀	340	220 ⁺¹⁴⁰ ₋₁₅₀	380
T _{atms} (K)	150 ⁺¹⁶⁰ ₋₈₀	120	200 ⁺³⁰⁰ ₋₁₄₀	40
X _{HCN}	-8.9 ^{+1.0} _{-0.6}	-8.0	-11.1 ^{+1.1} _{-1.3}	-9.9
PA (°)	70.0 ^{+1.4} _{-1.7}	70.8	135 ⁺¹⁶ ₋₁₆	136
q	1.0 ^{+0.7} _{-0.6}	0.8	[−0.5]	[−0.5]
ln Likelihood			-30928	

* Values in [brackets] were fixed for this run.

Table 4.6: MCMC Fitting Results (HCN); R_{out, B} < 250

Parameter	Disk A		Disk B	
	Median	Best Fit	Median	Best Fit
R _{out} (au)	470 ⁺¹⁶⁰ ₋₁₄₀	340	120 ⁺¹⁰⁰ ₋₇₀	150
T _{atms} (K)	170 ⁺¹⁷⁰ ₋₉₀	140	170 ⁺³²⁰ ₋₁₂₀	150
X _{HCN}	-9.0 ^{+0.9} _{-0.6}	-8.7	-10.8 ^{+1.4} _{-1.5}	-10.5
PA (°)	69.8 ^{+1.5} _{-1.5}	69.3	134 ⁺¹⁷ ₋₁₇	134
q	0.9 ^{+0.6} _{-0.7}	1.2	[−0.5]	[−0.5]
ln Likelihood			-30928	

* Values in [brackets] were fixed for this run.

4.3.3 CO(3-2) Fit

Finally, we fit the CO(3-2) line. Despite the removal of baselines below 60 kλ, the CO(3-2) line still shows significant cloud contamination in channels near the systemic velocity in the channel maps. In an attempt to keep the MCMC walkers

from trying to fit the contamination, we did not evaluate the χ^2 contribution of the channels with velocities between 9.88 and 12 km s^{-1} , which show the worst of the clouds' effects. However, since it seems that this range was insufficient, it would have been preferable to exclude a wider range of contaminated channels, likely from around 6.5 - 13.3 km s^{-1} . This will be implemented in future work.

Table 4.7: MCMC Fitting Results (CO)

Parameter	Disk A		Disk B	
	Median	Best Fit	Median	Best Fit
$R_{\text{out}}(\text{au})$	409^{+86}_{-130}	500	190^{+100}_{-70}	110
$T_{\text{atms}}(\text{K})$	178^{+261}_{-170}	5	290^{+170}_{-180}	510
$\log M_{\text{Disk}}(M_{\odot})$	$-2.3^{+2.1}_{-0.7}$	-0.1	$-4.9^{+0.4}_{-0.4}$	-4.9
PA ($^{\circ}$)	71^{+3}_{-3}	73	[136]	[136]
q	$0.1^{+0.4}_{-0.6}$	0.3	[-0.5]	[-0.5]
ln Likelihood			-33577	

* Values in [brackets] were fixed for this run.

As a result, the fits are noticeably less certain than those of the HCO+ and HCN lines, featuring several jagged and bimodal posteriors, shown in Fig.4.5. Additionally, since the best-fit values disagree significantly with the results from the other lines (particularly in the T_{atms} for disk A, which is unrealistically low), we are unable to include these results in our analysis.

4.4 Reflections on the Fits

If the CO fits had converged to physical values, we would have used its disk mass results in the other runs, but since these results are not to be trusted, we instead continued to use the disks' mass values presented in Williams et al. (2014), which were inferred from continuum emission.

The HCO⁺and HCN runs converged into impressive agreement, although the posteriors from the HCO⁺line show smaller uncertainties than those of the HCN line. Both the HCO⁺and HCN lines show molecular abundances in disk A that are almost two orders of magnitude than those in disk B (discussed in §5). The two lines' fits for disk A's outer radius agree to within around 1% (although the HCN fit is significantly less certain than the HCO⁺fit) and the lines' best-fit q values agree to within 15%. Atmospheric temperatures for disk A in both lines are large and significantly different, with the HCO⁺line preferring a temperature 50% greater than HCN's, but this is at least somewhat expected, as the two molecules are emitting from different regions of the disk and thus could reflect different regions of its temperature profile. In both lines, disk A's temperature structure power law index, q , is atypically positive compared to both theoretical and observed literature values (see §5), although we expect this parameter to not settle with absolute certainty, since the observations do not have enough spatial resolution to constrain it tightly.

Fits for disk B are systematically less well constrained, primarily in outer radius. This likely reflects the fact that it is smaller, unresolved, and more easily overrun by emission from features that were not modeled, such as cloud contamination, excess disk A emission, and tidal interactions between the two disks. The outer radius was most notably affected by these features, yielding somewhat bimodal posteriors in both HCO⁺and HCN as the walkers sometimes tried to fit the outer features. As discussed in §4.3.2, a posteriori cuts of the HCN model's MCMC chain limiting disk B's outer radius to ≥ 250 au - in effect, manually choosing one of the posterior's two modes - changed the best-fit parameters significantly, most notably leading the HCN fit's value for disk B's outer radius and temperature into agreement with HCO⁺. This likely indicates that the MCMC walkers were trying

to fit the tidal features connecting the two disks; in future work, we will consider how best to restrain them from doing this with the use of priors.

Finally, the resulting best-fit temperature and density structures for each line are plotted in Fig. 4.7

Visualizing HCN Model Radius Fits

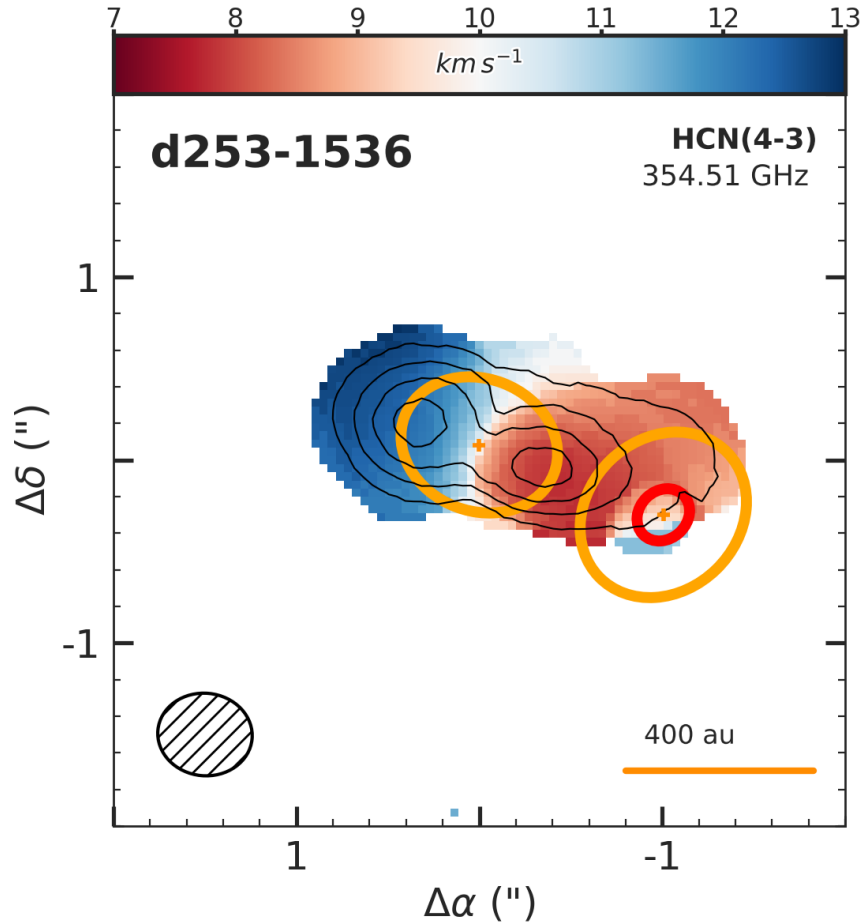


Figure 4.2: Zeroth (contours) and first (color) moment maps of HCN emission, overlaid with ellipses described by each disk's best-fit position angle, inclination, and outer radius. For disk B, both the best-fit outer radius with and without the 250 AU a posteriori prior implemented (at 324 and 145 AU, respectively) are plotted.

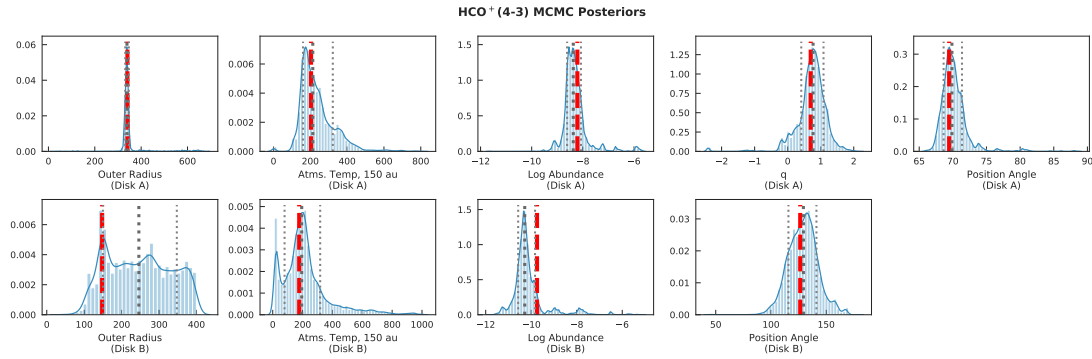


Figure 4.3: Posteriors of results from MCMC fitting of HCO⁺ emission, where the grey dotted lines represent median $\pm 1\sigma$ and the red dashed line represents best fit, as given in 4.4. The fits are generally good.

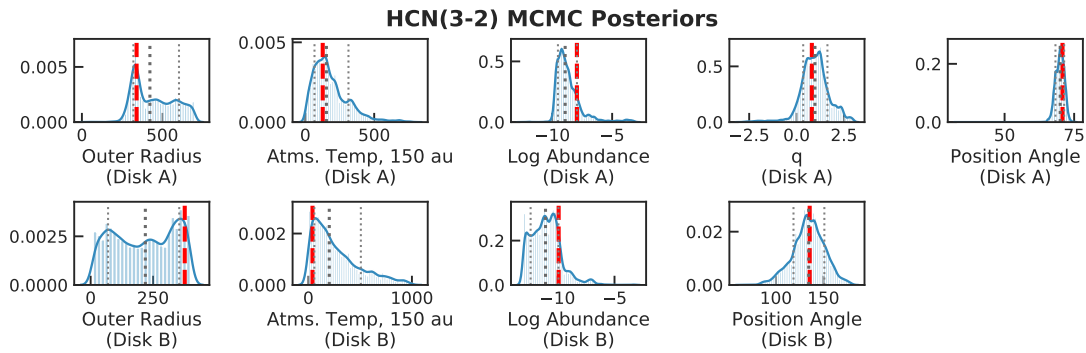


Figure 4.4: Posteriors of results from MCMC fitting of HCN emission, where the grey dotted lines represent median $\pm 1\sigma$ and the red dashed line represents best fit, as given in 4.6. The fits are generally good, albeit somewhat wide-spread. Of particular note is the bimodal nature of disk B's radius fit, which is discussed in the text.

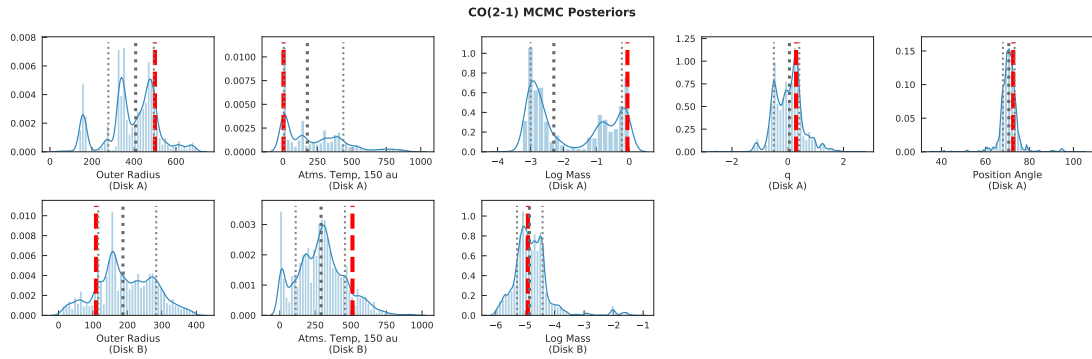


Figure 4.5: Posteriors of results from MCMC fitting of CO emission, where the grey dotted lines represent $\text{median} \pm 1\sigma$ and the red dashed line represents best fit, as given in 4.7. As discussed in the text, the MCMC algorithm had trouble with the CO fitting.

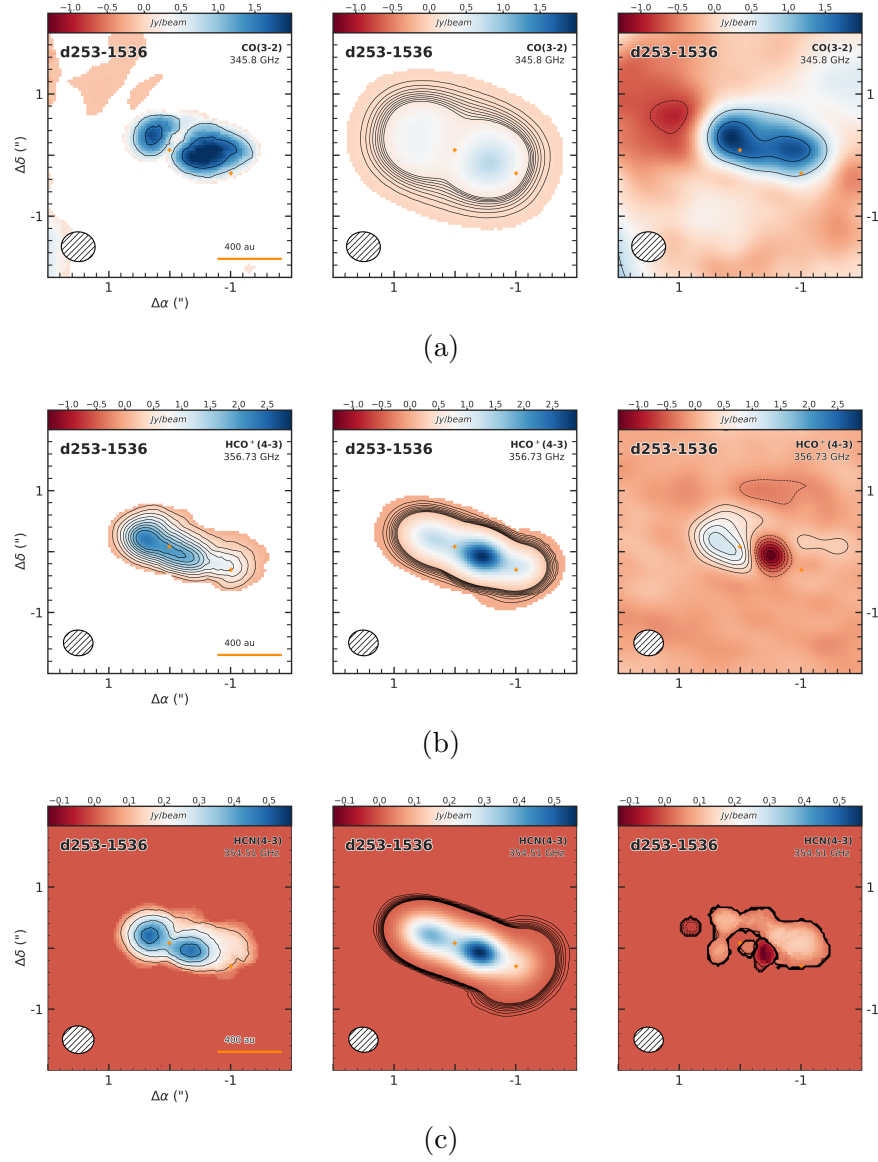


Figure 4.6: Triptychs of data (left), model (center), and residuals (right) for CO, HCO⁺, and HCN. Clearly, the fits are not yet perfect, but have the correct form. Of particular note is the HCN residual, which traces the region of interaction between the two disks.

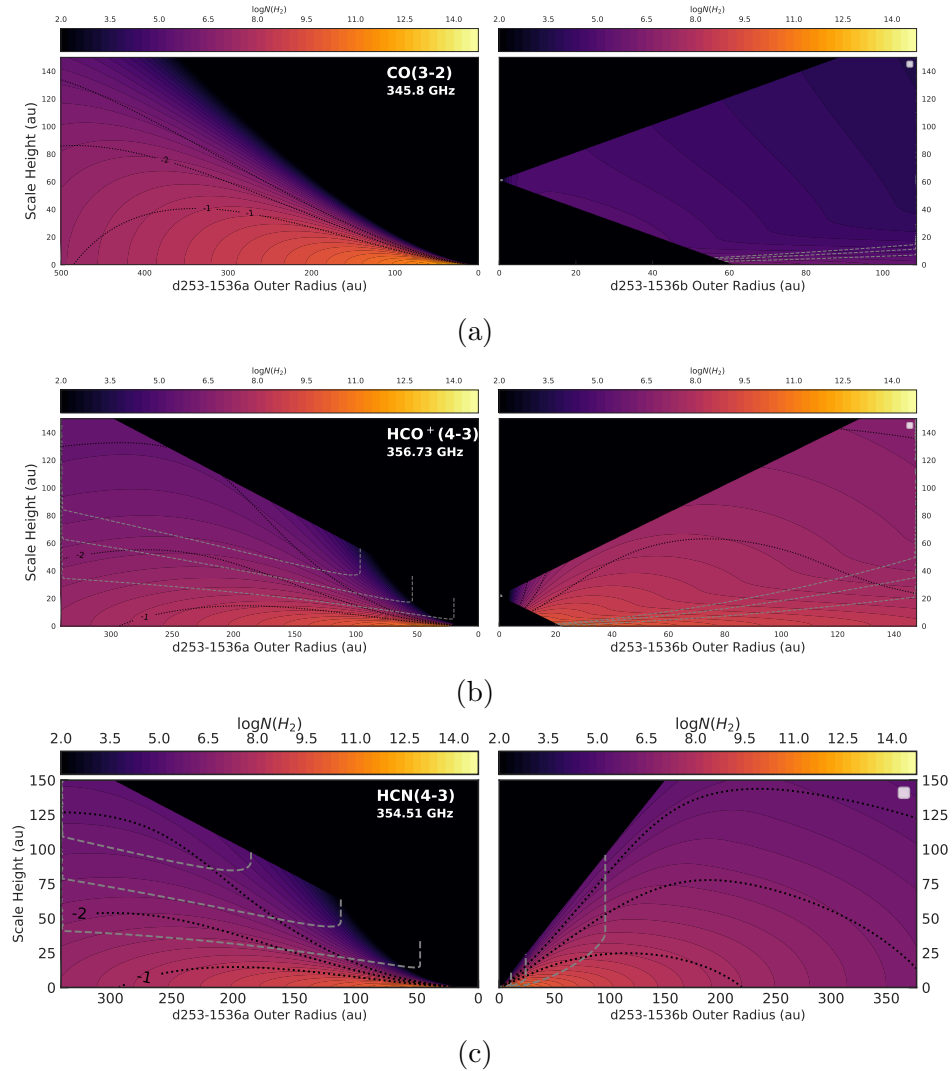


Figure 4.7: Density and temperature profiles for the best-fit models for CO, HCO⁺, and HCN show varied disk structures.

Chapter 5

Discussion

With the disks now fit, we may interpret our results. Since this project was framed around the question of how environment influences protoplanetary disks, we would like to compare our best fit values to other disks, including to one other from the ONC (Factor et al. 2017) as well as to disks in low-mass regions. We begin with a brief review of the relevant literature on the three disk profiles that we fit (densities, temperatures, and chemical abundances) so that we may frame our results in a meaningful context.

5.1 Physical Structure

To get a sense of how these disks' physical characteristics (i.e. mass and radius) compare to other protoplanetary disks, it is useful to compare our results to other disks in the Orion Nebula Cluster, as well as others in low-mass star forming regions (SFRs). It is again worth reiterating that many of the reported disk gas masses in the literature (as well as the values we use here from Williams et al. 2014) are calculated from continuum emission (which traces dust mass), and then scaled by the factor of 100 to return a gas mass. However, as briefly discussed in §1), this ISM-based gas/dust ratio has been shown to be neither constant across surveys disks nor best approximated by 100:1.

In an attempt to avoid relying on the use of the 100:1 gas/dust ratio, Williams

& Best (2014) presented a method to infer a disk’s gas mass by comparing ratios of CO isotopologues. This method involves developing parametric disk models over a wide range of parameters (similar to the modeling process that we use) and calculating the resulting emission intensities of selected lines (generally C¹⁸O and ¹³CO due to their relatively high abundances but lack of cloud contamination). By generating a large set - or “grid” - of models over a range of parameter values, observations of a disk can then be located on that grid, essentially through template fitting. In this process, they hold certain molecular and atomic abundance ratios fixed (most notably, their CO/H₂ ratio is held at the molecular cloud-level of 10⁻⁴). Their application of the method to nine well-studied disks in Taurus yielded masses appreciably lower than a 100:1 gas/dust ratio would have implied, instead returning a wide range of ratios that were centered around 10:1. Analysis of 89 disks in Lupus (Ansdell et al. 2016) using this method also showed a similar trend, although due to insufficient C¹⁸O detections, only 11 of the disks’ masses were able to be fully estimated, while another 25 had upper limits established.

Miotello et al. (2014), Miotello et al. (2016) and Miotello (2017) build on the methods of Williams & Best (2014), using CO isotopologue ratios to find gas mass, but avoid the use of fixed abundance ratios by integrating a full chemical-reaction network to simulate the effects of freeze-out and photodissociation (the two main effects driving chemical evolution), allowing the abundance ratios to self-equilibrate. With this addition, they were able to reanalyze and expand the sample of constrained gas masses from the Ansdell et al. (2016) survey from 11 to 34. Their results again show that the use of a fixed gas/dust ratio is inappropriate, and that 100:1 is typically far too high. Miotello (2017) notes that this deficiency could be the result either of an initial lack of gas, or could reflect a high rate of carbon depletion (through chemical evolution or lock-up in larger bodies), but

that these observations are insufficient to discern between these different scenarios.

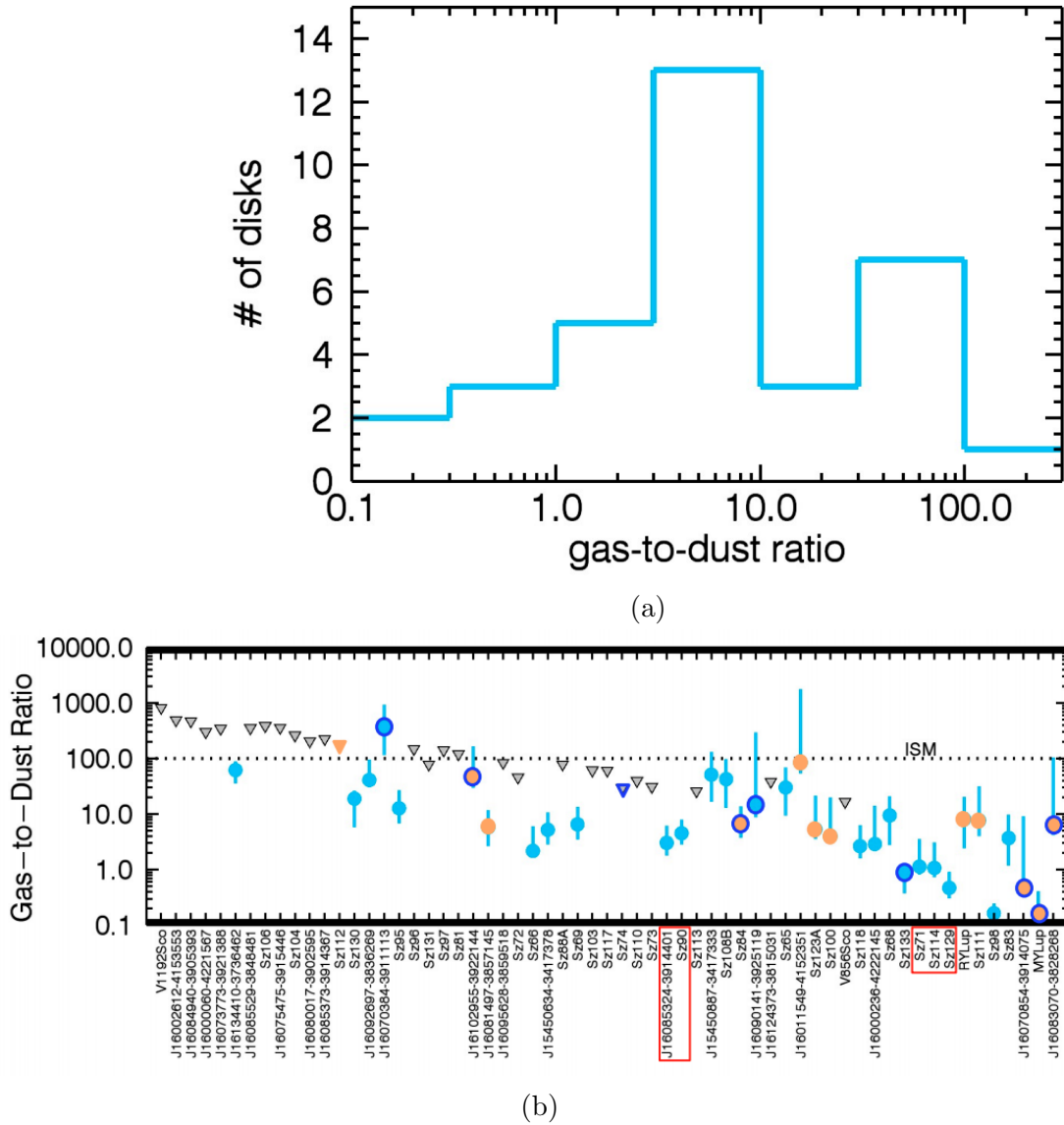


Figure 5.1: In their histogram of derived gas/dust ratios, Miotello (2017) show that the highest frequency ratio is closer to 10:1 than the ISM value of 100:1.

When calculating gas masses for the disks in d253-1536, Williams et al. (2014) found the disks' total dust masses from continuum emission and used the 100:1 gas/dust ratio discussed above to infer the gas masses. The uncertainty that this introduces, as well as the uncertainty from the actual flux measurement (noted in

§3), is crucial to keep in mind throughout the following analysis, as these factors imply that the reported gas masses are possibly up to an order of magnitude or two too large. A table of the disks' masses and radii, (as well as those from Factor et al. 2017, for comparison), are presented in Table 5.1 for reference throughout this chapter.

Table 5.1: Disk Parameter List

Disk	Radius ^a (au)	Radius ^b (au)	Gas Mass ^c (M _⊕)	Dust Mass ^d (M _⊕)
d253-1536a	340	268	7.5×10^{-2}	78.66
d253-1536b	148	-	2.9×10^{-2}	29.88
d216-0939	530	525	4.4×10^{-2}	145

^a Results of MCMC fitting of HCO⁺ emission.

^b Semi-major axis of 2D Gaussian fit to the disk's continuum emission (Mann et al. 2014)

^c Williams et al. (2014)

^d Since Williams et al. (2014) use a 100:1 gas/dust ratio, we may infer the dust emission to be two orders of magnitude lower than the gas.

The natural place to begin our comparison is with the survey of 22 ONC proplyds that originally provided these data (Mann et al. 2014). In it, the authors infer total disk masses and fit the disks with 2D elliptical Gaussians, and using the resulting semi-minor and -major axes of the disks as approximate measures of the disks' radial extents. Disk A in the present system was, by their measure, the most massive disk in the study, 75% (37σ) more massive than the study's next most massive disk, d216-0939 (the subject of Factor et al. 2017); disk B was the fifth most massive. Disk A had the study's fourth largest semi-major axis¹. The authors did not fit disk B's radial extent; however, our fit for its radius would

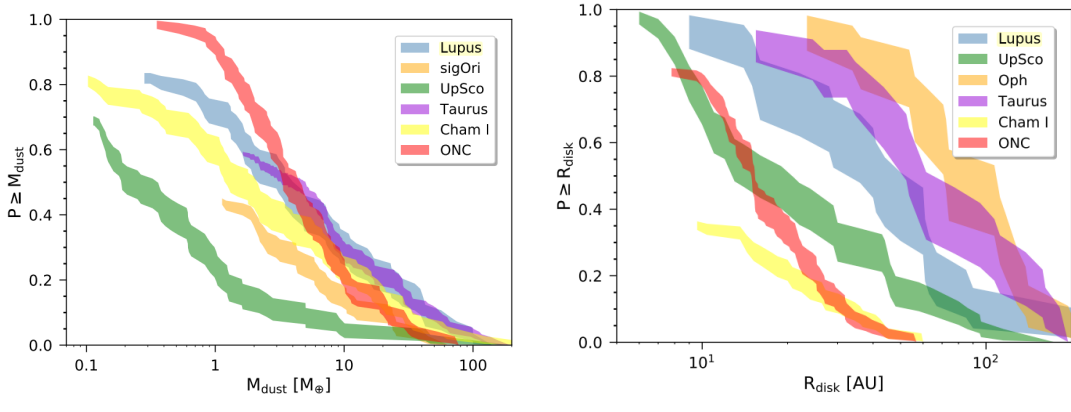
¹The authors' measurement of disk A's semi-major axis, at 268 au, is 2.6σ smaller than our fit measurements. The survey's reported semi-major axis for d216-0939 was also smaller than the fit value in Factor et al. (2017), though by less than 1σ . This may reflect the different radial extents of the gas and dust disks (see Hughes et al. 2008)

make it the eleventh largest (median radius) disk in the survey.

This work was followed by a survey of 104 detected disks in the heart of M42 within 0.14 pc of θ^1 Ori C (Eisner et al. 2018). The authors measure the disks’ dust masses (from continuum flux) and radii (again from fitting 2D elliptical Gaussians), and compare their distributions to similar measurements from other surveys of disks in low mass SFRs. These comparisons are summarized in Fig. 5.2 (see figure caption for references), showing the distributions of masses and radii of disks in each survey. From them, we see that these M42 disks are characteristically denser and radially truncated, as shown by the ONC track’s relatively high position on the mass plot and relatively low position on the radius plot. By locating our two disks on these plots, we find that their dust masses are far greater than the M42 disks and that disk A is more massive than any of the disks in all the surveys. However, while the ONC disks in this plot exhibit an atypically high density (the highest-mass disks have mass/radius ratios of around $1.5 M_{\oplus}/\text{au}$) relative to the other survey’s disks (which are closer to of order $0.5 M_{\oplus}/\text{au}$), disk A and B land at 0.75 and 0.65, respectively. This indicates that, while they are still somewhat more dense than the disks from low-mass SFRs, they show neither the radial truncation nor high densities found in the M42 disks; this is likely a result of their distance from the Trapezium cluster.

It is also worth noting that by using the methods described above to measure gas masses directly, Miotello (2017) found no disks more massive than $1.6 M_{\text{Jup}}$, while Ansdell et al. (2016) and Ansdell et al. (2018) found masses reaching no higher than $10 M_{\text{Jup}}$.

Andrews et al. (2013) showed that the masses of disks in Taurus are linearly correlated with the mass of their host stars, going as $M_{\text{disk}} \approx 0.4\% M_{\star}$ and ranging by up to a factor of 40. Our disks have masses approximately equal to 2% and 7%



(a) Disk mass distribution across surveys (b) Disk radius distribution across surveys

Figure 5.2: Comparing the distribution of masses and radii across surveys of different regions (Eisner et al. 2018) reveals that, while disks in the ONC have disk masses comparable to those of other regions, their radii are systematically truncated. *Survey References:* Lupus: Tazzari et al. (2017); σ Ori: Ansdell et al. (2017); Upper Sco: Barenfeld et al. (2017); Taurus & Ophiucus: Tripathi et al. (2017); Cham 1: Pascucci et al. (2016)

of their host stars for disk A and B, respectively, which is consistent with their linear fit and the associated uncertainty.

With the results of these surveys as context, we see that the disks in the d253-1536 binary have large radii and that their reported masses are extremely large, yielding densities that are higher than disks in low-mass SFRs but not as high as others in the ONC. However, due to the uncertainty in the mass measurement (both from the assumed gas/dust ratio and the uncertainty in locating the edges of each disk's flux boundary due to their overlap), the masses could be significantly less massive than reported. It is also possible that they could be more massive (and dense) than their reported values, but since both sources of uncertainty trend towards under-estimation (Miotello 2017, showed that disks in Lupus were better represented by a 10:1 gas/dust ratio, and, as discussed in §3, the integrated flux measurement that yields the disks' dust masses is likely over-counting emission),

it is more likely that these values are too high than too low.

5.1.1 Comparison to Binaries

We must also consider the fact that our disks are in a binary. While this work is not meant to be a complete review of multiple star systems (for a more comprehensive review, see Duchêne & Kraus 2013), some review of the relevant literature is again warranted to frame our interpretation of the present system.

Binaries (and higher-order systems, which generally form as hierarchical pairs) are quite common, with around 30% of low- and intermediate mass Main Sequence stars presenting with companions; that number climbs to 70% for high mass stars (Sana et al. 2012), and surveys of younger, T Tauri stars in low-mass regions show even higher fractions, up to almost 80% in Taurus (Kraus et al. 2011), for example. However, regions of higher densities (like the ONC) seem to have the opposite effect, as Reipurth et al. (2007) found that the 781 sources within 60'' of θ Ori C contained only 69 multiple systems (with apparent separations between 67 and 675 au), yielding to a companion fraction of just 9%. There is notable subsetting within that population, particularly with a deficiency of wide (0.''5 - 1.''5, or around 200-600 au at the ONC's distance of 389 pc) binaries closer to θ_1 Ori C (see Fig. 5.3). Our binary, with an angular separation of 1.''1, represents one of the widest pairs in the ONC, and with $d = 591''$ is comfortably into the “flat” region of the radial distribution of binaries from θ_1 Ori C.

As one might expect, disks are not uncommon around disks in binaries. Several millimeter/sub-millimeter surveys have observed a number of disks in binary systems in various regions, most notably in Taurus and ρ Ophiucus. Since these regions are low-mass SFRs, they are qualitatively different environments than the

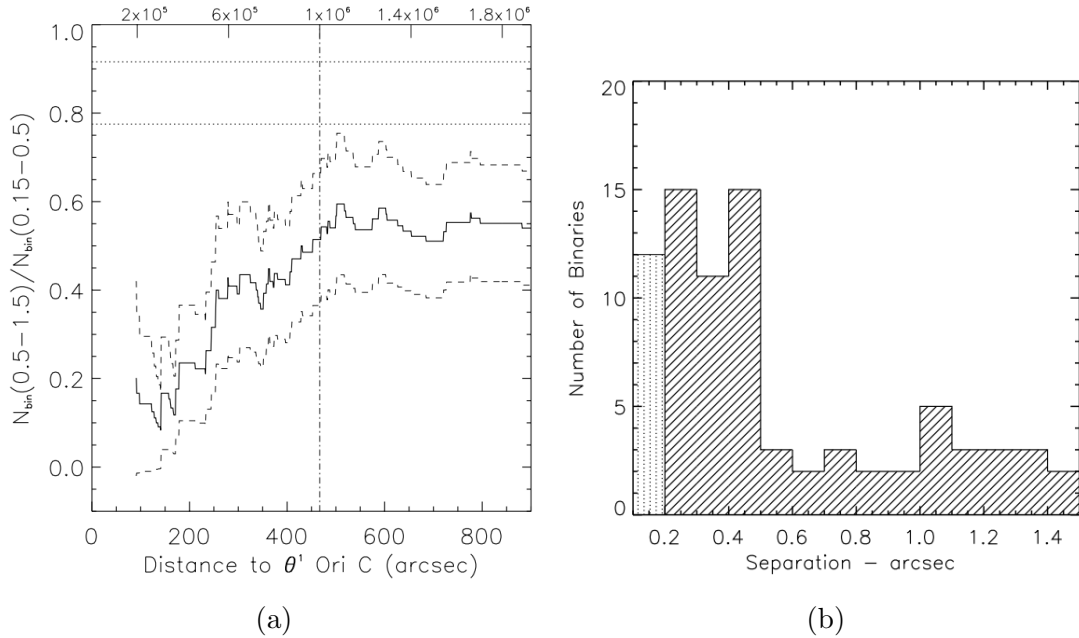


Figure 5.3: Statistics for binary pairs in the Orion Nebula Cluster (Reipurth et al. 2007). In (a), the vertical dotted line represents the point at which the distribution becomes flat. The present system is around 591" from θ_1 Ori C, putting it beyond the radius apparently affected by the massive star.

ONC, but provide us with a good starting point to compare to.

Harris et al. (2012) observed disks in 23 multiple-star systems in Taurus using the Submillimeter Array. In it, they found a strong anticorrelation between system brightness and projected separation between components, with wide pairs (>300 au) showing similar brightness to that of two single stars, while tight pairs (<30 au) suffer a $5\times$ decrease from the equivalent sum of individual brightnesses (although the presence of circumbinary disks around binaries of any separation make the system significantly brighter; see Fig.5.4). Akeson et al. (2019) built on these results with an ALMA survey of additional binaries in Taurus, developing a sample of 151 sources with resolved millimeter detections, 99 of which were in binary systems. From this sample, they found that disks around the binaries' primary (more massive) star contribute, on average, 62% of the disks' total com-

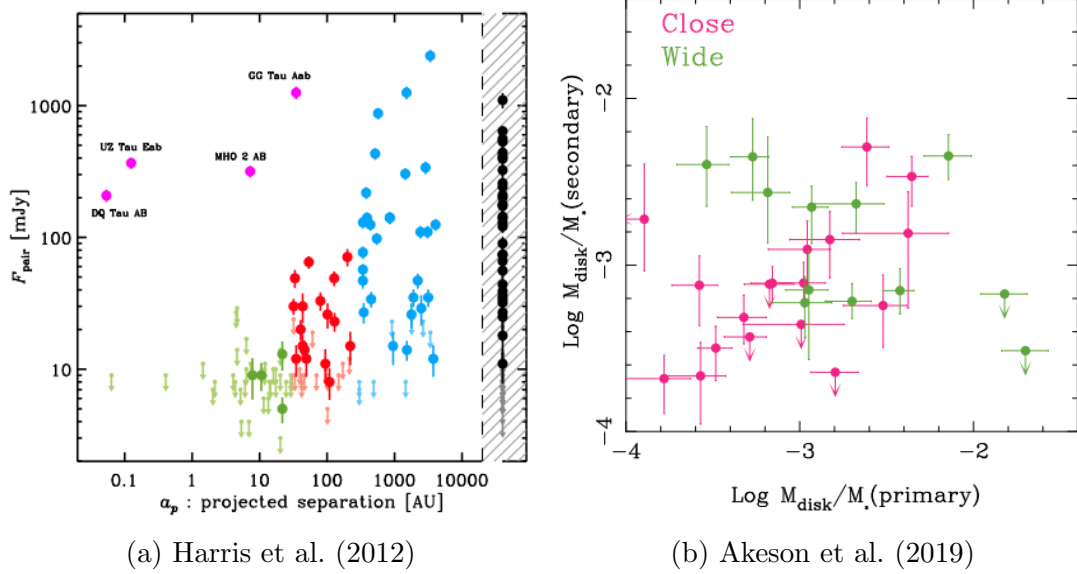


Figure 5.4: Population trends from binary pairs in the Taurus star-forming region. (a): There is a clear upper limit on pair flux that is correlated to projected separation (green, red, and blue marks represent close, medium, and wide pairs). the presence of a circumbinary disk (magenta) yields an extra source of flux, and so pairs featuring such a disk do not follow the separation-limited flux pattern. (b): The mass of the disk around the secondary member of the binary in close systems (pink) is correlated to the mass of the primary, while in wide systems (green), the two are anti-correlated.

bined mass, although this distribution has a wide spread. They also developed the observation by Harris et al. (2012) (and previously in Jensen 1996) that tighter binaries led to lower fluxes, finding that, as a function of stellar mass, disks in binaries have systematically lower masses than their isolated counterparts, and that this mass truncation is more apparent in tighter binaries (see Fig. 5.4). They found that $M_{\text{disk}}/M_{\star}$ for the primary and secondary stars are correlated in close systems but anticorrelated in wide systems, and that the rough correlation between disk mass and stellar mass shown in Andrews et al. (2013) did not hold in their sample. Finally, they note that the absence of a significant population of circumbinary disks in the sample suggests that they are either not common or

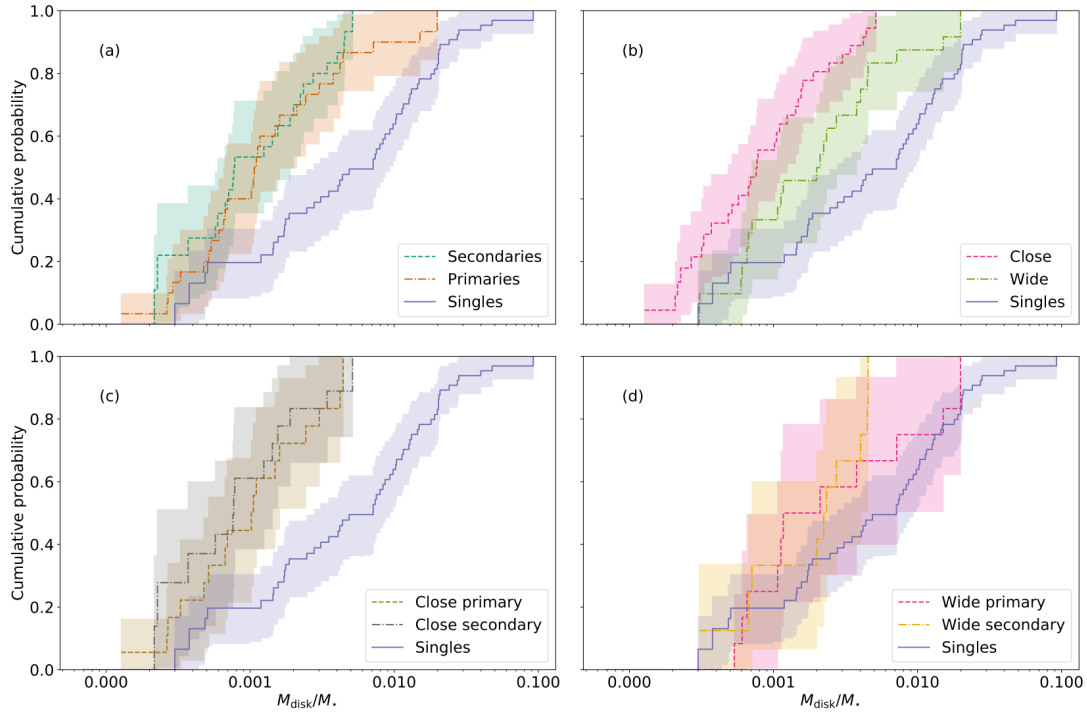


Figure 5.5: Cumulative probabilities of disk masses for different combinations of disks in binary pairs (Akeson et al. 2019). (a): Both disks in binary pairs are systematically less massive than single (isolated) disks although, as expected, the primary has more representation at the more massive end. (b): Close pairs are more significantly truncated than wide pairs, although wide pairs are still undermassive as well. (c) Close pairs do not preferentially truncate either disk; each has a sharp upper limit. (d): Primaries in wide pairs have nearly the same mass probability as single disks.

quickly (<1 - 2 Myr) dissipated.

Disks in binary pairs have also been surveyed in the ρ Ophiucus region. Akeson & Jensen (2014) studied 17 pairs with separations ranging from 100-990 au using ALMA, measuring the systems' masses. In it, they found no correlation between disk mass and stellar mass, matching the results from the studies of Taurus binaries above. Cox et al. (2017) followed with a survey targeting 63 total sources, comprised of 11 binaries, three triple systems, and 34 single sources. In it, they, like Harris et al. (2012) and Akeson et al. (2019), found significantly

lower fluxes from sources in binaries than isolated ones, and found that the disks' radii also exhibited systematic truncation. They note that this truncation is likely either due to tidal interactions between the disks or reflects a natural limit on the radii of disks in binaries, inherent to the disks' formation process, and that these decreased fluxes can be generally interpreted as being proportional to decreased masses. They also found no correlation between the ratios of the stellar masses and the ratios of the disk masses in the sample, indicating that environmental factors that are shared by both components are likely not a dominant factor in determining disk masses.

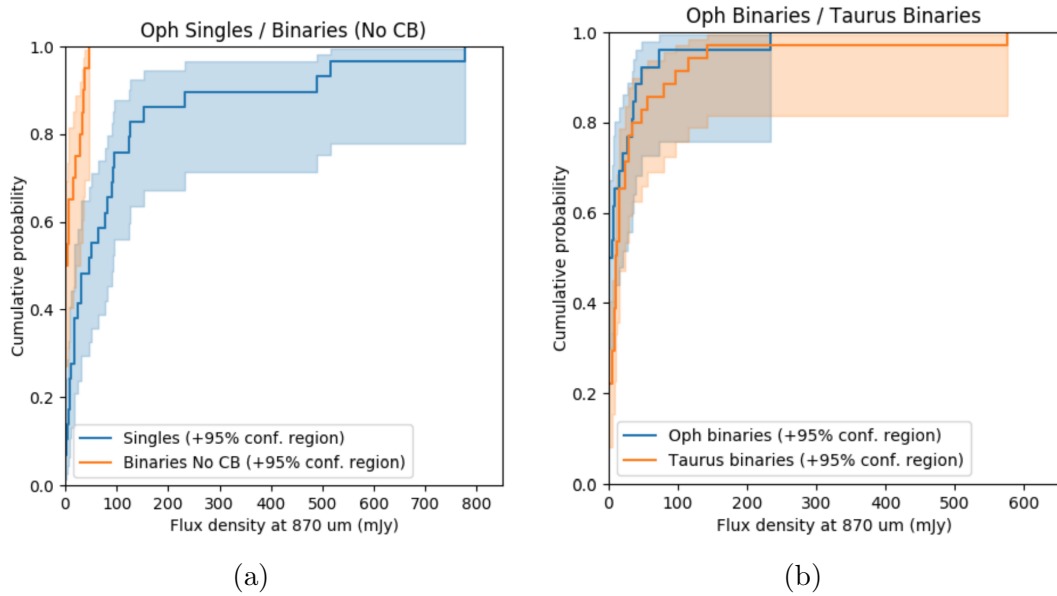


Figure 5.6: Cox et al. (2017) showed that disks in binary systems (excluding circumbinary disks) in ρ Ophiucus have systematically lower fluxes than both isolated disks in the region (*left*) and disks in binaries in Taurus *right*.

Comparing the this thesis's binary pair to these surveys immediately shows that its disks are neither faint nor small, neither in comparison to the disks in those surveys or to the disks in the survey that it was a part of. However, this is not out of line from the morphological patterns presented in the surveys above

since, at 428 au, the disks' projected separation is enough to put them beyond the reach of the most significant mass and radius truncations that are typical of closer binaries, and its large distance from θ^1 Ori C likewise protects it.

5.2 Chemical Structures

We now explore the chemical nature of protoplanetary disks. These disks have strong radial and vertical gradients in their temperatures, densities, and radiation fields, creating a wide range of chemistries. These chemistries can be broadly divided into inner- and outer-disk regimes, thanks to exponential radial temperature decay (Dartois et al. 2003). Inner disk temps are high and thus best suited to IR observations, while outer disks are cold and better suited to sub-millimeter observations. Because our investigation is rooted in ALMA data, we will review the outer disk here. Working with the basic building blocks of hydrogen, nitrogen, oxygen, and carbon and a wide diversity of temperature, density, turbulence, and radiation environments, disks can develop an array of molecules in their outer regions, each with its own characteristic formation conditions and emission signatures. Understanding disk chemistry is a process of knowing which of these signatures to look for and how to make sense of what they are telling us.

Since disks form out of molecular clouds, the abundances found there should provide reasonable initial guesses for our disks' chemical abundances. Aikawa et al. (1999) showed these to be (for the molecules that we model) $X_{HCO^+} = 9 \times 10^{-9}$ and $X_{HCN} = 2 \times 10^{-8}$. However, since disks undergo complex chemical evolution, developing a parametric understanding of the chemical structure and evolution of protoplanetary disks guides our interpretation of data. Below is a brief overview of some of the efforts that have been made to do so.

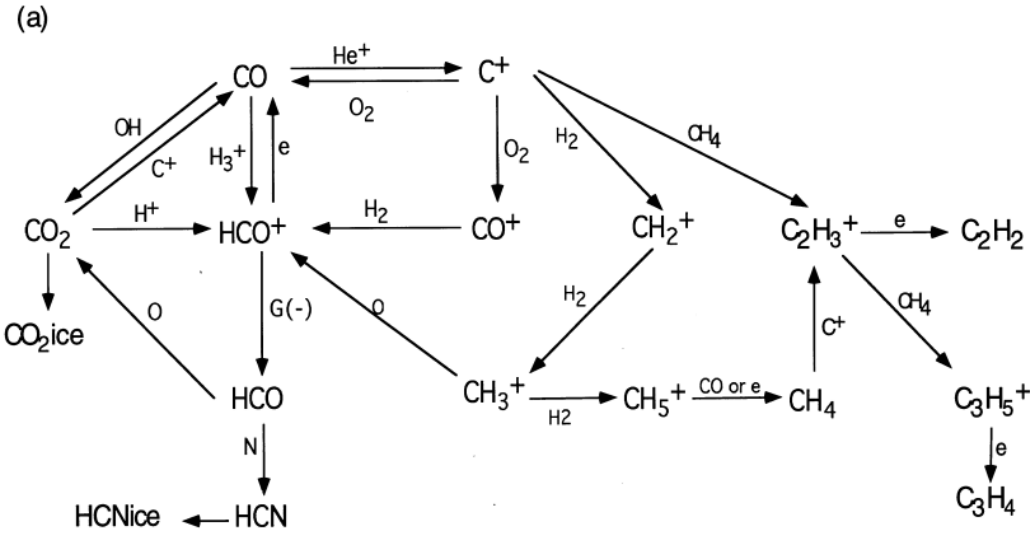


Figure 5.7: The chemical process leading to the generation of HCO⁺ and HCN (Aikawa et al. 1999). We immediately see that the generation of HCO⁺ is directly dependent on CO, while that same HCO⁺ molecule can then combine with N to yield the disk's HCN.

Aikawa et al. (1997) were some of the first to apply time-evolving chemical networks to protoplanetary disks, describing a radial model of the effects of cosmic rays in the outer disk and how they can convert CO and N₂ (which together dominate the disk's initial composition) into more complex organics, including HCN, through chemically active ions (Fig. 5.7). Aikawa et al. (1999) expanded on the work, modeling the evolution of molecular abundances in an accreting protoplanetary disk. They show that the timescale of this chemical evolution is dependent on the disk's ionization rate and the size distribution of the dust grains, increasing with lower ionization rates and/or larger grains and vice versa. As grains grow, HCN abundances are lowered by orders of magnitude, since they depend heavily on the grain surface recombination rates of HCO⁺ (Aikawa & Herbst 1999a), which are significantly smaller in the case of larger grains. Aikawa & Herbst (1999b) and Aikawa et al. (2002) added a vertical dependence to the model, first with den-

sity and then with temperature, producing a full (r, z) description of chemical evolution of a protoplanetary disk's temperature and density profiles and calculating the resulting interactions between the gas and dust, X-rays, and cosmic rays. They found that ionization in the mid-plane is driven by cosmic rays, while at significant heights from the midplane, X-rays from the central star also become a major ionizing source. These efforts yielded approximately radially constant distributions of HCO^+ and HCN, with HCO^+ presenting column densities about an order of magnitude above those of HCN (a reversal from the molecular cloud's conditions). These results highlighted the role of ionization in protoplanetary disks and the need for a more complete description of the effects of high-energy radiation - both from the central star and cosmic rays, across a wide range of energies - on the evolution of their gas masses.

In Fogel et al. (2011), the authors show how strong radiation fields (i.e. from neighboring massive stars) will have the effect of amplifying the disk's natural CO-based photo-chemistry (already driven by the host star) and increase the size of the disk's warm gas layer. Additionally, the disk's dust evolution can affect the gas (Fogel et al. 2011; Akimkin et al. 2013), with grain growth and sedimentation leading to decreased UV shielding of the disk's inner layers and pushing the disk's molecular layer closer to the midplane. As the grains grow larger, their total surface area decreases, making gas-grain collisions less frequent. These interactions are crucial for the evolution of HCO^+ (and, consequently, HCN), as Aikawa & Herbst (1999a) show. The decreased surface area also offers less attenuation of incoming rays, ultimately slowing molecular freezeout. This, in turn, leads to heightened column densities for many species, including CO and HCN.

To study the effects of this ionization in anticipation of the arrival of ALMA,

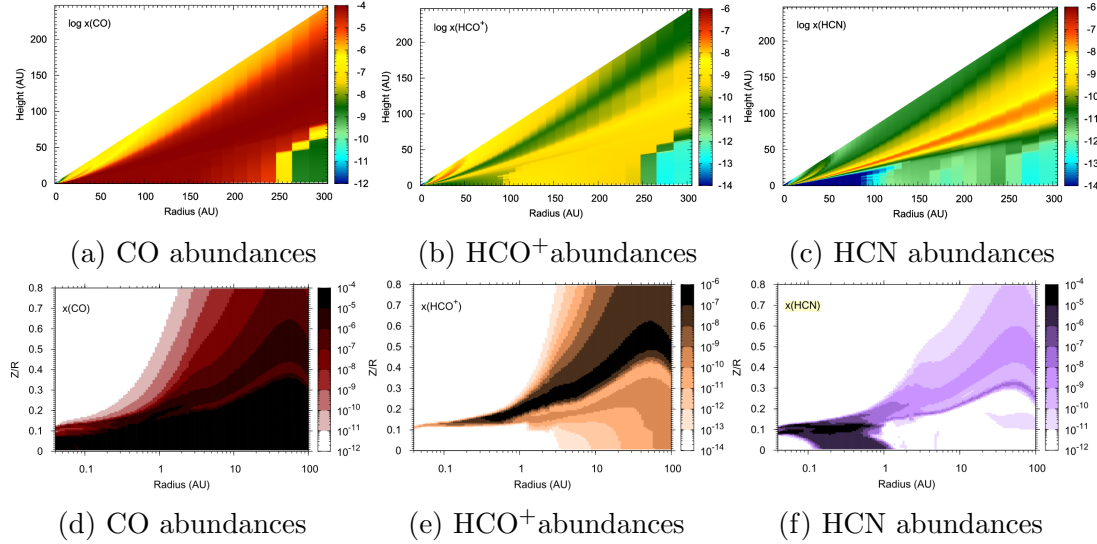


Figure 5.8: Models showing radial and vertical distributions of CO, HCO^+ , and HCN in a simulated disk around a T-Tauri star. The top row shows the profiles of isolated disks (Walsh et al. 2010), while the bottom row shows the profiles of disks being irradiated by a nearby O star (Walsh et al. 2013). Note that bottom row is on a log scale and only covers the inner 100 AU of the disk, while the top row is linearly scaled and shows a 300AU stretch.

Walsh et al. (2010) developed radial and vertical chemical models for an isolated protoplanetary disk around a T-Tauri star, tracing molecular abundance distributions throughout the disk for molecules within ALMA’s reach. They showed that log abundances in their models for HCO^+ varied from -8 to -12 , -7 to -12 for HCN, and -4 to -9 for CO, all of which are consistent with our fits. The authors then built on this model by adding functionality to model externally-driven UV and X-ray ionization (Walsh et al. 2012) and applied it to the same disk system, this time with an O star nearby providing ionizing photons (Walsh et al. 2013) and again mapped the resulting molecular abundance distribution (see Fig. 5.8). The authors note that, in their externally photoionized disk, HCO^+ column density increases by a factor of 6.3 relative to the isolated disk, whereas HCN and CO column densities remain constant through ionization. They also note that the

ionized disks have much higher gas temperatures, $T \gg 50$ K; this is consistent with the high temperatures that we see in our disks.

Cleeves et al. (2013, 2014) also modeled the radiation and ionization environment in these disks, developing models to compare the relative contributions of stellar UV, stellar X-rays, and cosmic rays (see Fig.5.9). They found that stellar winds could disrupt cosmic rays and lowering their ionization rates by orders of magnitude. Their findings showed that HCO^+ can trace high cosmic ray (CR) rates, with its abundances dropping significantly with decreased CR contributions, thanks to its precursor, CO, freezing out in regions where CRs are the primary energy source but deficient. They also note that HCO^+ abundances can suffer from particularly high UV fluxes (from either Herbig host stars or high radiation environments), as CO can be photodissociated before having a chance to form HCO^+ .

On the temperature side, we expect in an ideal disk to find $q = -0.5$ (recalling that the radial temperature structure is generally assumed to go as $T(r) \propto r^q$). Such a structure invokes the assumption of a smooth, consistent distribution of emitting material, so variations from that value indicate variations in the structure. Studies of individual disks (in low-mass SFRs) have largely been in line with this prediction, ranging from -0.22 (Flaherty et al. 2015) to -0.7 (?). In their study of another ONC proplyd, Factor et al. (2017) found that their HCN emission traced a moderately-high structure of $q = -0.18$, but that their HCO^+ line showed $q = 0.17$. Schwarz et al. (2016) note that a flatter or non-negative structures are to be expected when observing emission that originates from layers just above freeze out temperature in the disk.

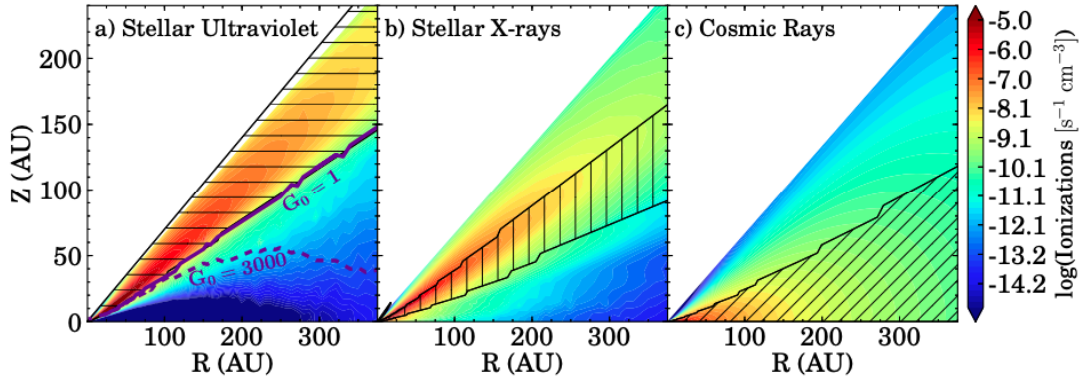


Figure 5.9: Radiation contribution on a protoplanetary disk from stellar UV, stellar X-rays, and cosmic rays (Cleeves et al. 2013). (a): The $G_0 = 1$ contour represents the effects from a host-only UV field (i.e. an isolated star), while the $G_0 = 3000$ contour represents the effects of a UV field made up of both the host as well as from the interstellar radiation field. Fatuzzo & Adams (2008) showed 3000 to be a typical value for G_0 in clusters. While the specific radiation field around these disks is unknown, Pabst et al. (2019) showed that they are in a region of $G_0 \geq 50$, indicating that they are likely in a field somewhere between the two contours. (b): Stellar X-rays are shown to dominate the inner regions of the disk, where the warm-molecular layer is and where HCN likely resides. Since d253-1536b is an actively accreting M star, it likely has X-ray flaring. (c):

5.3 Implications

With this context, how do now we make sense of our current observations and fits? Our results show a wide (428 au separation) binary pair of stars with disks that are massive² and radially large (both compared to other disks in the ONC and disks in binaries in Taurus and ρ Ophiucus). The two disks have appreciably different chemistries, and are physically interacting, as shown by the HCN residuals.

Since our disk model produces a single, flat relative abundance for each molecule across the disk, we are inherently unable to resolve the level of detail presented in the models. However, we may use their predictions to inform tentative in-

²Although this mass is, of course, still handicapped by the assumptions about gas/dust ratios.

terpretations of our results. According to Walsh et al. (2013), HCO⁺ is a tracer of cold, dense material and is generally more abundant in the outer midplane, whereas HCN follows warmer material closer in to the disk’s center (since it is non-volatile, it freezes out more easily). In their models of an isolated disk, the line strength (in units of mJy km s⁻¹) ratio of HCN/HCO⁺ is 27.1/54.1 (0.50), while in an irradiated disk it is 71.9/86.9 (0.83). Using the line strengths that we reported in §3, we find in disk A’s ratio to be 0.69/4.15 (0.17) and disk B’s at 0.26/0.80 (0.33), significantly lower even than the isolated disk. This could help explain the unexpectedly high q value that our MCMC walkers settled on, as, in agreement with the Walsh et al. (2013) prediction above, these would imply that HCO⁺ is extremely abundant and that that mass is stored in the disks’ outer reaches, forcing the temperature profile to flip to compensate for the flux farther out to compensate for a flat abundance. This is also consistent with the Schwarz et al. (2016) observation that a high q value would reflect emission from layers just above freeze out, since that is where HCO⁺ is predicted to be.

This casts our interpretation of the abundances in an interesting light. It is somewhat uncertain to what degree they should be trusted since, if the explanation above is correct, then a flat abundance structure is likely a bad approximation for these disks. However, we still do see interesting features in these numbers which are worth exploring. As shown in §3, disk A’s ratio of log abundances between HCN and HCO⁺, $X_{\text{HCN}}/X_{\text{HCO}^+}$, is 8/8.2, while disk B’s is 9.9/9.8. The fact that both disks present a nearly identical ratios but that the abundances are separated by nearly two-orders of magnitude seems to reflect some difference in structure between the two disks.

One immediate explanation for this variation in overall abundance between disks could be found by recalling that the two disks are hosted by very differ-

ent stars: d253-1536a is an F or G star, and nearly nine times as massive as d253-1536b, an accreting M-star. It is possible that one star could have stronger emission at an energy that affects both molecules equally, either depleting or enhancing both together and yielding the observed discrepancy.

Another way to increase abundances, as described above, is through dust grain growth/dust depletion, as the resulting decrease in the dust's total surface area leads to both decreased shielding and decreased area for gas-grain interactions and slowing molecular freeze out. This relative dust mass can be approximated with a quick density calculation of M_{dust}/r , which for disk A yields $78/341 = 0.23 \text{ M}_{\text{Jup}}/\text{au}$ and $30/148 = 0.20 \text{ M}_{\text{Jup}}/\text{au}$ for disk B. However, since these values are quite close and given the significant uncertainties in the mass measurements, a more nuanced study would be needed to pursue this approach further. Still, it would seem that this is a potentially useful path to follow: Ricci et al. (2011) predict, through modeling of the binary's SEDS from the VLA, that disk A should have larger dust grains, which would help begin to explain its elevated abundances. Another dust-related explanation could be that bodies too large for ALMA to see (from pebbles to planets) may be depleting one disk's gas mass, as proposed by Miotello et al. (2016). Whether this would be a chemically-selective depletion (e.g. whether or not it would affect both HCO^+ and HCN evenly) is unclear, but should be considered a possibility.

A less probable but still fascinating possibility is that these disks did not form together. Williams et al. (2014) posit that wide binaries (systems with separations $\geq 300 \text{ au}$) such as this one do not form in the same initial cloud structures. If this were the case, then it might be reasonable to expect each disk to reflect different chemistries of the regions in which each star formed. However, binary capture is rare, as a third star is required for this process to create a bound pair (e.g.

Mansbach 1970), and it is unclear whether the local stellar environment shows history of such an event. It is also unclear how the binary's stellar mass ratio - around 9:1 - would affect the capture process, as such captures usually involve mass ratios closer to unity.

It is clear, in any case, that these disks show appreciable deviation from our standard assumptions about the physical and chemical structures of protoplanetary disks.

Chapter 6

Summary

We have presented ALMA observations tracing line emission CO(3-2), HCO⁺(4-3), HCN(4-3), and CS(7-6) of d253-1536, a wide-separation binary system containing two young circumstellar protoplanetary disks in the M43 region of the Orion Nebula Cluster. We model the HCO⁺, HCN, and CO emission using a gas model that assumes Keplerian rotation, local thermodynamic equilibrium, and hydrostatic equilibrium to develop synthetic images of a binary of model disks. We then use an affine-invariant Markov Chain Monte Carlo (MCMC) algorithm to explore parameter space and identify regions of best fit, comparing each model image to our data using a χ^2 test. By fitting each line's emission, we are able to statistically characterize elements of the disks' chemical compositions and their temperature structures.

We find atmospheric temperatures that are atypically high relative to studies of other protoplanetary disks, as well as a temperature structure that increases radially, which is inconsistent with past studies of disks in low-mass star forming regions. Additionally, we find that in disk A, the binary's eastern disk, HCO⁺ and HCN abundances are nearly two orders of magnitude higher than in disk B, although the ratio of the molecules' abundances are almost exactly equal (near unity) in both disks. Finally, we note that the ratios of each molecule's integrated line flux in both disks is significantly lower than those predicted to be found in

either an isolated disk or an irradiated disk (Walsh et al. 2013), perhaps reflecting a radially-dependent mass distribution for the different chemical species.

We also compared these results to results from Factor et al. (2017), the only other forward-modeled study of line emission from an ONC proplyd. Our disks did not share the high abundance of HCN that they found, but their HCO⁺line did match our large and radially-increasing temperatures. These deviations from literature (based on studies of disks in low-mass SFRs) hint at the potential for systematic variations between disks in low and high mass regions, and emphasize the need for further study of disks in the Orion Nebula Cluster.

Bibliography

- Aikawa, Y., & Herbst, E. 1999a, *Astrophys. J.*, 10, 262
- . 1999b, *Astron. Astrophys.*
- Aikawa, Y., Umebayashi, T., Nakano, T., & Miyama, S. M. 1997, *Astrophys. Journal, Suppl. Ser.*
- . 1999, *Astrophys. J.*, 10
- Aikawa, Y., van Zadelhoff, G. J., van Dishoeck, E. F., & Herbst, E. 2002, *Astron. Astrophys.*, 386, 622
- Akeson, R. L., & Jensen, E. L. N. 2014, *Astrophys. J.*, 784
- Akeson, R. L., Jensen, E. L. N., Carpenter, J., Ricci, L., Laos, S., Nogueira, N. F., & Suen-Lewis, E. M. 2019, *Astrophys. J.*
- Akimkin, V., Zhukovska, S., Wiebe, D., Semenov, D., Pavlyuchenkov, Y., Vasyunin, A., Birnstiel, T., & Henning, T. 2013, *Astrophys. J.*, 766
- Anderson, K. R., Adams, F. C., & Calvet, N. 2013, *Astrophys. J.*, 774
- Andrews, S. M., et al. 2018, *Astrophys. J. Lett.*
- Andrews, S. M., Rosenfeld, K. A., Kraus, A. L., & Wilner, D. J. 2013, *Astrophys. J.*, 771
- Andrews, S. M., & Williams, J. P. 2005, *Astrophys. J.*, 631, 1134
- . 2007, *Astrophys. J.*, 1

- Andrews, S. M., Wilner, D. J., Hughes, A. M., Qi, C., & Dullemond, C. P. 2009, *Astrophys. J.*, 700, 1502
- Ansdel, M., Williams, J. P., Manara, C. F., Miotello, A., Facchini, S., van der Marel, N., Testi, L., & van Dishoeck, E. F. 2017, *Astron. J.*, 153, 240
- Ansdel, M., et al. 2018, *Astrophys. J.*
- . 2016, *Astrophys. J.*
- Barenfeld, S. A., Carpenter, J. M., Sargent, A. I., Isella, A., & Ricci, L. 2017, *Astrophys. J.*, 851, 85
- Bontemps, S., et al. 2001, *Astron. Astrophys.*
- Bosman, A. D., van Dishoeck, E. F., & Walsh, C. 2018, *Astron. Astrophys.*
- Butler, B. 2012, ALMA Memo 594
- Chapillon, E. 2013, New Trends Radio Astron. ALMA Era
- Chapillon, E., Guilloteau, S., Dutrey, A., & Piétu, V. 2008, *Astron. Astrophys.*, 488, 565
- Chiang, E., & Laughlin, G. 2013, *Mon. Not. R. Astron. Soc.*, 431, 3444
- Cieza, L. A., et al. 2019, *Mon. Not. R. Astron. Soc.*, 482, 698
- Cleeves, L. I., Adams, F. C., & Bergin, E. A. 2013, *Astrophys. J.*, 772
- Cleeves, L. I., Bergin, E. A., & Adams, F. C. 2014, *Astrophys. J.*, 794
- Cleeves, L. I., Bergin, E. A., Bethell, T. J., Calvet, N., Fogel, J. K. J., Sauter, J., & Wolf, S. 2011, *Astrophys. J. Lett.*, 743, 1

- Cleeves, L. I., Bergin, E. A., Qi, C., Adams, F. C., & Öberg, K. I. 2015, *Astrophys. J.*, 799
- Collaboration, T. E. H. T. 2019, *Astrophys. J.*, 1
- Combes, F., et al. 2018, *Astron. Astrophys.*, 79, 1
- Cox, E. G., et al. 2017
- Dartois, E., Dutrey, A., & Guilloteau, S. 2003, *Astron. Astrophys.*, 399, 773
- de Gregorio-Monsalvo, I., et al. 2013, *Astron. Astrophys.*, 557, A133
- Duchêne, G., & Kraus, A. 2013, *Annu. Rev. Astron. Astrophys.*, 1
- Dullemond, C. P., & Monnier, J. D. 2010, *Annu. Rev. Astron. Astrophys.*, 1
- Dutrey, A., et al. 2014, *Nature*, 514, 600
- Dutrey, A., Guilloteau, S., & Gu, M. 1997, *Astron. Astrophys.*, 317, 55
- Eisner, J. A., et al. 2018, *Astrophys. J.*
- Eistrup, C., Walsh, C., & van Dishoeck, E. F. 2017, *Astron. Astrophys.*
- F. Shu, F. Adams, S. L. 1987, *Annu. Rev. Astron. Astrophys.*
- Factor, S. M., et al. 2017, *Astrophys. J.*
- Fatuzzo, M., & Adams, F. C. 2008, *Astrophys. J.*, 675, 1361
- Flaherty, K. M., et al. 2017, 163296, 1
- Flaherty, K. M., Hughes, A. M., Rosenfeld, K. A., Andrews, S. M., Chiang, E., Simon, J. B., Kerzner, S., & Wilner, D. J. 2015, *Astrophys. J.*, 813, 1

- Flaherty, K. M., Hughes, A. M., Teague, R., Simon, J. B., Andrews, S. M., & Wilner, D. J. 2018, 1
- Fogel, J. K., Bethell, T. J., Bergin, E. A., Calvet, N., & Semenov, D. 2011, *Astrophys. J.*, 726
- Foreman-Mackey, D., Hogg, D. W., Lang, D., & Goodman, J. 2013, *Publ. Astron. Soc. Pacific*
- Gaia Collaboration. 2016, *Astron. Astrophys.*
- Gaia Collaboration, Brown, A. G. A., Vallenari, A., Prusti, T., de Bruijne, J. H. J., Babusiaux, C., & Bailer-Jones, C. A. L. 2018, *Astron. Astrophys.*
- Gaidos, E., Krot, A. N., Williams, J. P., & Raymond, S. N. 2009, *Astrophys. J.*, 696, 1854
- Goodman, J., & Weare, J. 2010, *Math. Sci. Publ.*, 5, 1
- Harris, R. J., Andrews, S. M., Wilner, D. J., & Kraus, A. L. 2012, *Astrophys. J.*, 751, 1
- Hartmann, L., Calvet, N., Gullbring, E., & D'Alessio, P. 1998, *Astrophys. J.*, 741
- Haworth, T. J., Boué, D., Facchini, S., Bisbas, T. G., & Clarke, C. J. 2016, *Mon. Not. R. Astron. Soc.*, 463, 3616
- Henney, W. J., & O'Dell, C. R. 1999, *Astron. J.*, 118, 2350
- Henning, T., & Semenov, D. 2013
- Herrera-Martín, A., Hendry, M., Gonzalez-Morales, A. X., & Ureña-López, L. A. 2019, *Astrophys. J.*, 872, 11

- Hildebrand, R. 1983, Q. J. R. Astron. Soc., 24, 267
- Hogbom, J. 1974, Astron. Astrophys. Suppl.
- Hubickyj, O., Bodenheimer, P., & Lissauer, J. J. 2005, Icarus, 179, 415
- Hughes, A. M. 2010, PhD thesis, Harvard University
- Hughes, A. M., Duchene, G., & Matthews, B. 2018, Annu. Rev. Astron. Astrophys., 1
- Hughes, A. M., et al. 2017, Astrophys. J., 839, 86
- Hughes, A. M., Wilner, D. J., Qi, C., & Hogerheijde, M. R. 2008, Astrophys. J.
- Isella, A., Testi, L., Natta, A., Neri, R., Wilner, D., & Qi, C. 2007, Astron. Astrophys., 469, 213
- Jensen, E. L., & Akeson, R. 2014, Nature, 511, 567
- Jensen, E. L. N. 1996, Phd, Arizona State University
- Johnstone, D., Hollenbach, D., & Bally, J. 1998, Astrophys. J., 499, 758
- Kalyaan, A., Desch, S. J., & Monga, N. 2015, Astrophys. J., 815, 112
- Kenyon, S. J., Gomez, M., & Whitney, B. A. 2008, Handb. Star Form. Reg. Vol. I, I
- Kraus, A. L., Ireland, M. J., Martinache, F., & Hillenbrand, L. A. 2011, Astrophys. J., 731
- Kruijssen, J. M. D., & Longmore, S. N. 2019, 1
- Kuchner, M. J. 2004, Astrophys. J., 612, 1147

- Lada, C. J., & Lada, E. A. 2003, *Annu. Rev. Astron. Astrophys.*, 57
- Lai, D. 2014
- Liu, Y., et al. 2018, 75, 1
- Luhman, K. L., Allen, P. R., Espaillat, C., Hartmann, L., & Calvet, N. 2010, *Astrophys. Journal, Suppl. Ser.*, 186, 111
- Lynden-Bell, D., & Pringle, J. E. 1974, *Mon. Not. R. Astron. Soc.*, 168, 603
- Mann, R. K., Andrews, S. M., Eisner, J. A., Williams, J. P., Meyer, M. R., Di Francesco, J., Carpenter, J. M., & Johnstone, D. 2015, *Astrophys. J.*, 802, 1
- Mann, R. K., et al. 2014, *Astrophys. J.*, 784, 1
- Mann, R. K., & Williams, J. P. 2009, *Astrophys. J.*, 699, 1994
- Mansbach, P. 1970, *Astrophys. J.*
- McKee, C. F., & Ostriker, E. C. 2007, *Annu. Rev. Astron. Astrophys.*, 565
- McKinney, W. 2010, *Proc. 9th Python Sci. Conf.*, 1697900, 50
- . 2011, 19, 583
- McMullin, J. P., Waters, B., Schiebel, D., Young, W., & Golap, K. 2007, *Astron. Soc. Pacific Conf. Ser.*, 376, 127
- Miotello, A. 2017, *Proc. Int. Astron. Union*, 13, 124
- Miotello, A., Bruderer, S., & van Dishoeck, E. F. 2014, *Astron. Astrophys.*, 572, A96

- Miotello, A., van Dishoeck, E. F., Kama, M., & Bruderer, S. 2016, *Astron. Astrophys.*, 594, A85
- Observatory, A. ????, *Origins — ALMA*
- Offner, S., Kratter, K., Matzner, C., Krumholz, M., & Klein, R. 2011, *Am. Astron. Soc. Meet. Abstr.* 217, 43, 258
- Ovelar, M. d. J., Kruijssen, J. M. D., Bressert, E., Testi, L., Bastian, N., & Cabrera, H. C. 2012, 1, 1
- Pabst, C., et al. 2019, Disruption of the Orion molecular core 1 by wind from the massive star $\theta 1$ Orionis C
- Panić, O., Hogerheijde, M. R., Wilner, D., & Qi, C. 2008, *Astron. Astrophys.*, 491, 219
- Panić, O., van Dishoeck, E. F., Hogerheijde, M. R., Belloche, A., Güsten, R., Boland, W., & Baryshev, A. 2010, *Astron. Astrophys.*, 519, A110
- Pascucci, I., et al. 2016, *Astrophys. J.*, 125
- Pavlyuchenkov, Y., Semenov, D., Henning, T., Guilloteau, S., Pietu, V., Launhardt, R., & Dutrey, A. 2007, *Astrophys. J.*, 669, 1262
- Podio, L., et al. 2019, *Astron. Astrophys.*, 6, 1
- Qi, C., D'Alessio, P., Berg, K. I., Wilner, D. J., Hughes, A. M., Andrews, S. M., & Ayala, S. 2011, *Astrophys. J.*, 740
- Qi, C., et al. 2004, *Astrophys. J.*, 616, L11
- Raymond, S. N., & Cossou, C. 2014, *Mon. Not. R. Astron. Soc. Lett.*, 440

- Reboussin, L., Wakelam, V., Guilloteau, S., Hersant, F., & Dutrey, A. 2015, *Astron. Astrophys.*, 579, A82
- Reggiani, M., Robberto, M., Da Rio, N., Meyer, M. R., Soderblom, D. R., & Ricci, L. 2011, *Astron. Astrophys.*, 534, A83
- Reipurth, B., Guimarães, M. M., Connelley, M. S., & Bally, J. 2007, *Astron. J.*, 134, 2272
- Ricci, L., Robberto, M., & Soderblom, D. R. 2008, *Astron. J.*, 136, 2136
- Ricci, L., Testi, L., Williams, J. P., Mann, R. K., & Birnstiel, T. 2011, *Astrophys. J. Lett.*, 739, 1
- Robberto, M., et al. 2013, *Astrophys. Journal, Suppl. Ser.*, 207
- Rosenfeld, K. A., Andrews, S. M., Hughes, A. M., Wilner, D. J., & Qi, C. 2013, *Astrophys. J.*, 774
- Rosenfeld, K. A., Andrews, S. M., Wilner, D. J., & Stempels, H. 2012, *Astrophys. J.*, 806
- Salyk, C., Pontoppidan, K., Corder, S., Muñoz, D., Zhang, K., & Blake, G. A. 2014, *Astrophys. J.*, 792
- Sana, H., et al. 2012, *Science* (80-.), 337, 444
- Sault, R. J., Teuben, P. J., & Wright, M. C. H. 1995, *Astron. Data Anal. Softw. Syst.*
- Schöier, F. L., van der Tak, F. F. S., van Dishoeck, E. F., & Black, J. H. 2005, *Astron. Astrophys.*, 432, 369

- Schwarz, K. R., Bergin, E. A., Cleeves, L. I., Blake, G. A., Zhang, K., Öberg, K. I., van Dishoeck, E. F., & Qi, C. 2016, *Astrophys. J.*, 0, 1
- Skilling, J., & Bryan, R. K. 1984, *Mon. Not. R. Astron. Soc.*, 211, 111
- Smith, N., Bally, J., Licht, D., & Walawender, J. 2005, *Astron. J.*, 129, 382
- Tachibana, S., Huss, G. R., Kita, N. T., Shimoda, G., & Morishita, Y. 2006, *Astrophys. J.*, 639, L87
- Tazzari, M., et al. 2017, *Astron. Astrophys.*
- Tripathi, A., Andrews, S. M., Birnstiel, T., & Wilner, D. J. 2017, *Astrophys. J.*, 1
- Tsiganis, K., Gomes, R., Morbidelli, A., & Levison, H. F. 2005, *Nature*, 435, 459
- Van Der Walt, S., Colbert, S. C., & Varoquaux, G. 2011, *Comput. Sci. Eng.*, 13, 22
- van Dishoeck, E. F., & Blake, G. A. 1998, *Astron. Astrophys.*
- Vicente, S. M., & Alves, J. 2005, in *Astron. Astrophys.*, Vol. 205, 214–216
- Walsh, C., et al. 2016, *Astrophys. J.*, 823, L10
- Walsh, C., Millar, T. J., & Nomura, H. 2010, *Astrophys. J.*, 722, 1607
- . 2013, *Astrophys. J. Lett.*, 766, 1
- Walsh, C., Nomura, H., Millar, T. J., & Aikawa, Y. 2012, *Astrophys. J.*, 747
- Walsh, K. J., Morbidelli, A., Raymond, S. N., O'Brien, D. P., & Mandell, A. M. 2011, *Nature*, 475, 206

- Weidenschilling, S. 1977, *Astrophys. Space Sci.*
- Werneck, S. J., & D'Addario, L. R. 1977, *IEEE Trans. Signal Process.*, 39, 1478
- Williams, J. P., & Best, W. M. J. 2014, *Astrophys. J.*, 788
- Williams, J. P., Cieza, L., Hales, A., Ansdell, M., Ruiz-Rodriguez, D., Casassus, S., Perez, S., & Zurlo, A. 2019, *Astrophys. J. Lett.*, 1
- Williams, J. P., & Cieza, L. A. 2011, *Astrophys. J.*
- Williams, J. P., et al. 2014, *Annu. Rev. Astron. Astrophys.*, 796
- Xiao, L., & Chang, Q. 2018, *Astrophys. J.*, 853, 22
- Yu, M., Evans, N. J., Dodson-Robinson, S. E., Willacy, K., & Turner, N. J. 2017, *Astrophys. J.*, 1
- Zhang, K., Bergin, E. A., Blake, G. A., Cleeves, L. I., & Schwarz, K. R. 2017, *Nat. Astron.*, 1